



Kent Academic Repository

Newman, Daniel, Young, Lorna E., Waring, Thomas, Brown, Louise, Wolanska, Katarzyna I., MacDonald, Ewan, Charles-Orszag, Arthur, Goult, Benjamin T, Caswell, Patrick T., Sakuma, Tetsushi and others (2023) *3D matrix adhesion feedback controls nuclear force coupling to drive invasive cell migration*. *Cell Reports*, 42 (12). ISSN 2211-1247.

Downloaded from

<https://kar.kent.ac.uk/104307/> The University of Kent's Academic Repository KAR

The version of record is available from

<https://doi.org/10.1016/j.celrep.2023.113554>

This document version

Publisher pdf

DOI for this version

Licence for this version

CC BY (Attribution)

Additional information

Versions of research works

Versions of Record

If this version is the version of record, it is the same as the published version available on the publisher's web site. Cite as the published version.

Author Accepted Manuscripts

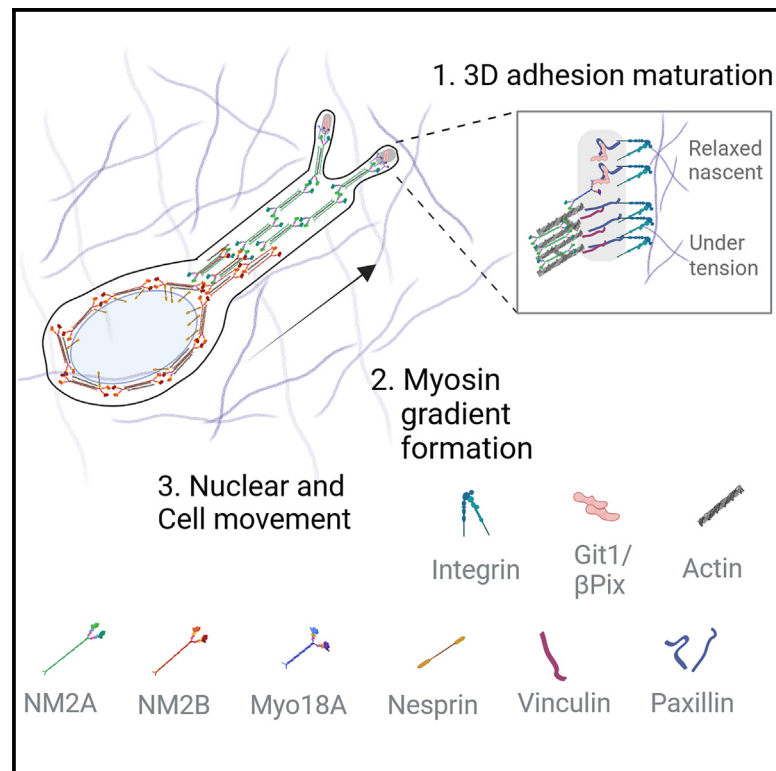
If this document is identified as the Author Accepted Manuscript it is the version after peer review but before type setting, copy editing or publisher branding. Cite as Surname, Initial. (Year) 'Title of article'. To be published in **Title of Journal**, Volume and issue numbers [peer-reviewed accepted version]. Available at: DOI or URL (Accessed: date).

Enquiries

If you have questions about this document contact ResearchSupport@kent.ac.uk. Please include the URL of the record in KAR. If you believe that your, or a third party's rights have been compromised through this document please see our [Take Down policy](https://www.kent.ac.uk/guides/kar-the-kent-academic-repository#policies) (available from <https://www.kent.ac.uk/guides/kar-the-kent-academic-repository#policies>).

3D matrix adhesion feedback controls nuclear force coupling to drive invasive cell migration

Graphical abstract



Authors

Daniel Newman, Lorna E. Young, Thomas Waring, ..., Laura M. Machesky, Mark R. Morgan, Tobias Zech

Correspondence

tzech@liverpool.ac.uk

In brief

Newman et al. define 3D cell-matrix adhesion composition and a pathway required for invasion in 3D matrix environments. βPix and Myo18A are required at cell adhesions to establish a polarized non-muscle myosin 2 isoform force-transduction network. This pathway is essential for nuclear movement and to drive cell migration through the matrix.

Highlights

- 3D cell-matrix adhesions share key nodes with 2D focal adhesions but have distinct features
- Cancer cell invasion requires mechanical integration between adhesion sites and the nucleus
- βPix and Myo18A are required to establish an NM2 isoform gradient between adhesions and nucleus
- Actomyosin force engagement displaces Git-βPix-Myo18A, establishing a feedback loop



Article

3D matrix adhesion feedback controls nuclear force coupling to drive invasive cell migration

Daniel Newman,¹ Lorna E. Young,¹ Thomas Waring,¹ Louise Brown,¹ Katarzyna I. Wolanska,¹ Ewan MacDonald,¹ Arthur Charles-Orszag,² Benjamin T. Goult,³ Patrick T. Caswell,⁴ Tetsushi Sakuma,⁵ Takashi Yamamoto,⁵ Laura M. Machesky,^{2,6,7} Mark R. Morgan,¹ and Tobias Zech^{1,8,*}

¹Institute of Systems, Molecular, and Integrative Biology, University of Liverpool, Liverpool, UK

²CRUK Beatson Institute, Garscube Estate, Switchback Road, Glasgow, UK

³School of Biosciences, University of Kent, Canterbury, UK

⁴Wellcome Trust Centre for Cell-Matrix Research, School of Biological Sciences, Faculty of Biology, Medicine, and Health, Manchester Academic Health Science Centre, University of Manchester, Manchester, UK

⁵Division of Integrated Sciences for Life, Graduate School of Integrated Sciences for Life, Hiroshima University, Hiroshima 739-8526, Japan

⁶Institute of Cancer Sciences, University of Glasgow, Garscube Estate, Switchback Road, Glasgow, UK

⁷Department of Biochemistry, University of Cambridge, 80 Tennis Court Road, Cambridge, UK

⁸Lead contact

*Correspondence: tzech@liverpool.ac.uk

<https://doi.org/10.1016/j.celrep.2023.113554>

SUMMARY

Cell invasion is a multi-step process, initiated by the acquisition of a migratory phenotype and the ability to move through complex 3D extracellular environments. We determine the composition of cell-matrix adhesion complexes of invasive breast cancer cells in 3D matrices and identify an interaction complex required for invasive migration. β Pix and myosin18A (Myo18A) drive polarized recruitment of non-muscle myosin 2A (NM2A) to adhesion complexes at the tips of protrusions. Actomyosin force engagement then displaces the Git1- β Pix complex from paxillin, establishing a feedback loop for adhesion maturation. We observe active force transmission to the nucleus during invasive migration that is needed to pull the nucleus forward. The recruitment of NM2A to adhesions creates a non-muscle myosin isoform gradient, which extends from the protrusion to the nucleus. We postulate that this gradient facilitates coupling of cell-matrix interactions at the protrusive cell front with nuclear movement, enabling effective invasive migration and front-rear cell polarity.

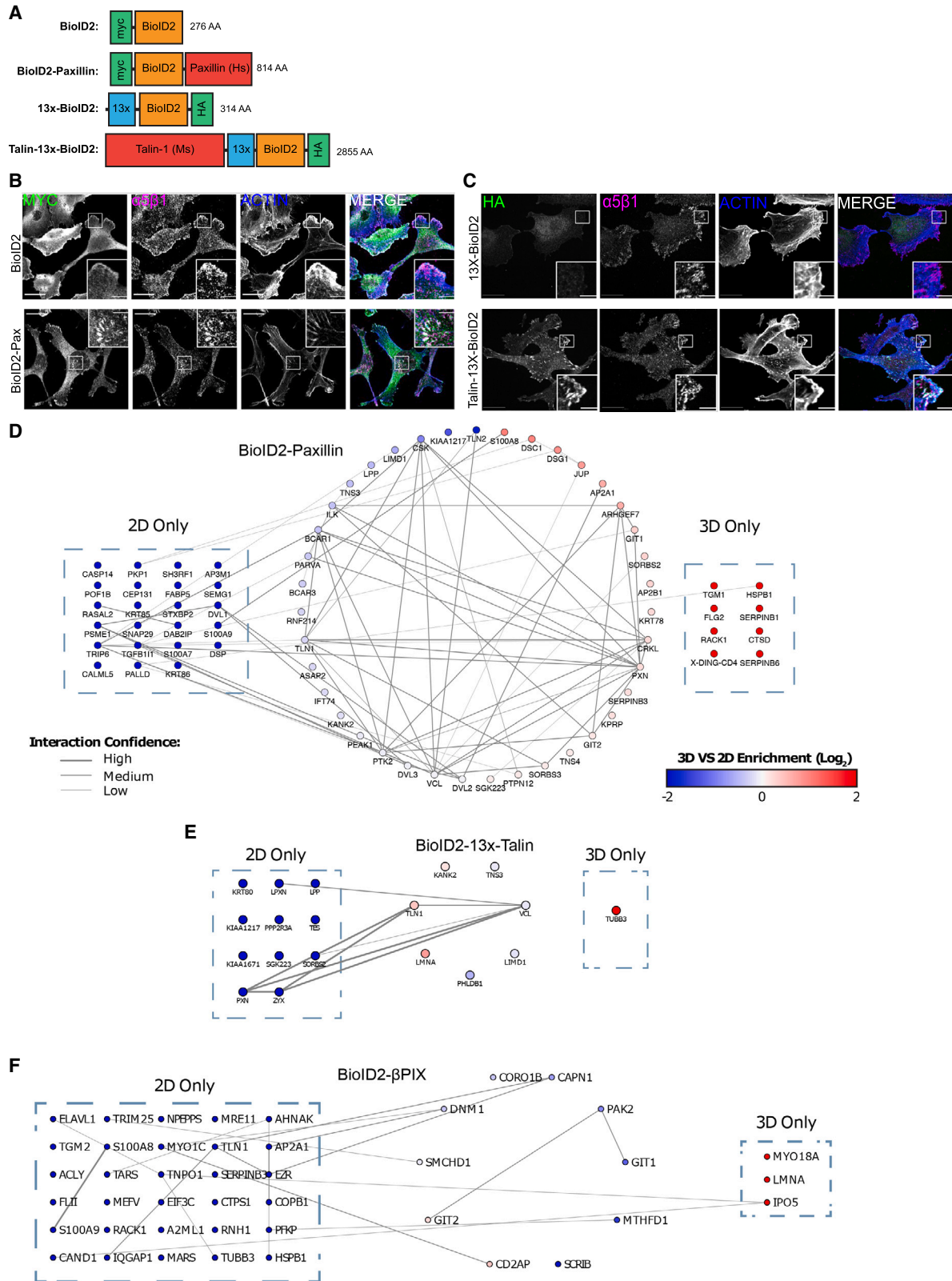
INTRODUCTION

Cell migration is fundamental for normal physiology and is dysregulated in many diseases, including cancer. Efficient migration depends critically on how cells sense and interact with their surrounding microenvironment and regulate cytoskeletal dynamics.^{1,2} Migrating cells interpret and influence the physical and biochemical properties of the extracellular matrix (ECM) as well as interact with neighboring/proximal cells. The mechanical and compositional properties of the ECM are detected primarily by membrane spanning integrin-associated adhesion complexes (IACs). IACs act as bidirectional signaling hubs, forming a mechanical link between the cytoskeleton and the ECM. A large number of proteins dynamically associate with IACs, changing over the life cycle of adhesion complexes and in response to their microenvironment. IACs formed on planar 2-dimensional (2D) substrates have been extensively studied using numerous techniques, including superresolution and live-cell microscopy, as well as biochemical isolation techniques.^{3–10}

These studies have provided great insight into the composition and regulation of IACs in 2D; however, biochemical isolation techniques such as immunoprecipitation are not readily transferable to cells in 3-dimensional (3D) culture, due to the large amount of matrix proteins that make sample handling and protein identification difficult.

There are few situations *in vivo* in which cells encounter a flat 2D environment. Instead, many non-hematopoietic cells are surrounded and functionally integrated with 3D ECM. A 3D microenvironment presents a number of challenges to migrating cells that are not present on 2D ECM substrates, including physical and topological cues and barriers. Compared with IACs on 2D substrates, little is known about the composition, regulation, and role of IACs in cells embedded in 3D microenvironments, but initial analyses of IACs in 3D matrix and *in vivo* suggest that they exhibit differences in composition, and are smaller in size in comparison with their 2D counterparts.^{11–13} More importantly, invasive cancer cells have hybrid adhesion structures in 3D, containing both the adhesion marker paxillin and the actin





(legend on next page)

polymerization factor N-WASP, often associated with invadopodial structures on 2D substrates.¹⁴ To date, technological limitations have prevented the comprehensive analysis of IAC signaling networks in 3D matrix.

IACs link the ECM to the cytoskeleton. Adaptor proteins such as talin and vinculin can bind both adhesion receptors and the actin cytoskeleton.^{15–19} IACs are involved in organizing actin into contractile actin networks containing non-muscle myosin 2 (NM2) bundles.^{20,21} In addition, IACs have several connections to actin polymerization factors via the recruitment of guanine nucleotide exchange factors (GEFs),²² WASP family members, and formins.^{23–25} The actin arrangement associated with newly formed—nascent—IACs is not well characterized and has been described as an actin “cloud” potentially polymerized by the transient recruitment of the Arp2/3 complex through FAK and vinculin.^{26,27} Mature adhesion complexes tend to be functionally connected to NM2-rich actomyosin stress fibers, whereas early/nascent adhesion has less associated NM2.²¹ The mechanism of this switch to NM2 association is currently unknown. Many cells express several NM2 isoforms with unique motor parameters and distinct functions.^{28–30} NM2 isoforms are not uniformly distributed throughout the cell, but do exhibit a polarized distribution.³¹ A gradient of NM2 isoforms is established, in which NM2A localizes predominantly to the cell periphery, whereas NM2B is concentrated more in the cell interior. Shutova and colleagues proposed a model whereby the prevalent recruitment of NM2A to the cell periphery is driven by its higher expression level, whereas the increased concentration of NM2B toward the cell interior is due to its stronger binding to polymerized actin.³² However, the function of the NM2 isoform gradient or its impact on invasive cell migration is unclear.

A major barrier to successful 3D migration is the ability of cells to move their nuclei through geometrically restrictive, densely cross-linked ECM.^{33–36} The outer nuclear membrane is coupled to the cytoskeletal network through the Linker of Nucleoskeleton and Cytoskeleton (LINC) complex.³⁷ The LINC complex contains the nesprin family of proteins, which connect to cytoskeletal components, and SUN domain proteins, which connect to the inner nuclear lamina.^{38,39} The complex therefore acts as a mechanical conduit bridging the outer cytoskeleton to the inner nucleoskeleton. Consequently, a functional LINC complex is critical for cell migration,^{36,40} nuclei movement, positioning and shape,^{41–43} and centrosome function and positioning,⁴⁴ and it is involved in force sensitive transcriptional pathways.⁴⁵

Despite the wealth of knowledge about cell migration, it is unclear how cells are able to couple nuclear movement with migration, and more important, what role IACs may play in this process, particularly during 3D migration. To investigate this, we developed an approach to directly compare IAC composition and signaling networks in 2D and 3D ECM using BioID2-based proximity-labeling coupled with proteomics.⁴⁶ We identify proteins in breast cancer cells that have not previously been associated with adhesions, a large number of proteins that are less abundant in 3D adhesions, and, critically, a defined group that exhibit enhanced enrichment in 3D adhesions, including β Pix and myosin18A (Myo18A). Downstream analysis revealed that β Pix and Myo18A are essential for efficient invasion without affecting the ability of the cell to form protrusions or degrade matrix. By contrast, β Pix and Myo18A control adhesion maturation and provide an active mechanism for the generation of the NM2A and NM2B isoform-gradient via recruitment of NM2A to the leading edge of protrusions. Failure to establish the membrane-nuclear NM2A/B gradient, either via perturbation to adhesions or the LINC complex, leads to the loss of nuclear force coupling, front-rear polarity, and 3D invasive migration.

Results identification of cell matrix adhesion networks in 3D environments

Previous proteomic studies have provided a comprehensive systematic analysis of IACs, predominantly from fibroblast cells, plated on 2D matrix substrates.⁴⁷ These analyses led to the definition of the “consensus adhesome,” a core set of proteins recruited to IACs, which were subdivided into four distinct signaling modules.⁴⁷ However, these proteomic strategies have not been used to analyze the composition of adhesions in invasive cancer cells embedded in 3D matrices.

To investigate the composition of IACs in invasive triple-negative breast cancer cells (MDA-MB-231), we developed an approach to compare adhesion protein complexes from 2D versus 3D extracellular matrices. We utilized a promiscuous biotin ligase-based proximity-dependent labeling approach, BioID2, which can label proteins within an approximately 10–20 nm range of the bait protein.⁴⁶ We generated two different BioID2 bait constructs fused to the consensus adhesome proteins paxillin (BioID2-paxillin; N-terminally labeled) and talin (talin-13x-BioID2; C-terminally labeled) (Figure 1A).⁴⁷ Paxillin and talin were chosen because both are known to act as scaffolding proteins and are associated with nascent as well as mature adhesions.^{48,49} More importantly, the respective N and

Figure 1. Comparison of IAC-associated proteins in MDA-MB-231 cells cultured in a 2D versus 3D microenvironment

- (A) Schematic of BioID2 adhesion constructs used in this study.
 (B) Immunostaining of MDA-MB-231 cell lines stably expressing BioID2 and BioID2-Paxillin on 2D substrates. Scale bars, 20 μ m (inset: 5 μ m).
 (C) Immunostaining of MDA-MB-231 cells stably expressing 13x-BioID2 or Talin-13x-BioID2. Scale bars, 20 μ m (inset: 5 μ m).
 (D and E) Protein-protein interaction network showing all of the proteins identified as being enriched in BioID2-Paxillin (D) or Talin-13x-BioID2 (E) compared with corresponding BioID2 control (Fisher exact, $p < 0.05$, Benjamini-Hochberg corrected) (N = 3). Interaction network obtained from STRING 10.5 (experimentally identified interactions only, confidence level >0.4). Protein enrichment is shown based on total spectral counts normalized to BioID2 identification in each condition. ECM proteins and common contaminants over-represented in CRAPome were removed from figure but are included in supplemental information.
 (F) A screen for interaction partners of β PIX conducted using MDA-MB-231 cells transiently transfected with BioID2- β PIX. Proteins were considered to be positively enriched if ≥ 3 spectra were identified and they were enriched 2-fold versus a BioID2-only expressing conditional control. Proteins identified in both 2D and 3D conditions are colored to represent 3D versus 2D total spectral counts normalized to total β PIX spectra for that given condition. Interaction network obtained from STRING 10.5 based on interaction database and experimental data. Edge weight represents interaction confidence score (high >0.95 , medium 0.95–0.9, low 0.9–0.4) (N = 1).

C termini of the two proteins have been reported to be localized at different axial strata within 2D adhesion complexes. Paxillin localizes close to the plasma membrane, whereas the C terminus of talin is distal from the membrane and positioned proximal to actin stress fibers.⁹

MDA-MB-231 cells stably expressing BioID2, BioID2-paxillin, and talin-13x-BioID2 were generated and verified (Figures 1B, 1C, S1A, and S1B). Cells were cultured either in 2D conditions—plastic dishes coated with fibronectin and collagen—or in 3D conditions—collagen hydrogels supplemented with fibronectin.

Following biotin treatment proteins were extracted, the biotinylated proteins enriched, analyzed by liquid chromatography-tandem mass spectrometry (MS) and subjected to statistical and network analysis. Within the BioID2-paxillin dataset, a total of 74 proteins (2D: 63, 3D: 51) were identified as significantly enriched across all 3 repeats compared to the BioID2-only control (Figures 1D; Data S1A–S1C). A total of 23 proteins were uniquely identified in 2D and 11 were present only in 3D, leaving 40 proteins that were identified in both conditions. By contrast, 20 proteins were identified in the talin1-13x-BioID2 dataset (2D: 18, 3D: 9, Figure 1E; Data S2A–S2C). A total of 11 proteins were identified in 2D and 2 were present only in 3D, whereas 7 proteins were identified in both conditions.

The biophysical properties of the cellular microenvironment are known to regulate gene expression. To examine whether the observed changes in protein detection between 2D and 3D culturing conditions were a result of changes in gene expression, RNA sequencing (RNA-seq) analysis was conducted on cells cultured using the same substrate conditions as those used in the proteomic datasets. Overall, no significant correlation was found between 3D and 2D gene expression in RNA-seq analysis and the 3D versus 2D enrichment of the identified hits in the BioID2-paxillin or talin1-13x-BioID2 datasets (Figures S1C–S1E). Seven proteins identified in the BioID2 datasets were found to have significant expression changes in the RNA-seq dataset, with only 4 proteins (RASAL2, HSPB1, SERPINB1, JUP) showing substantial changes in the same direction in both studies. This suggests that for the most part, within the BioID2 datasets, the changes in enrichment that were observed were largely independent of gene expression changes.

To estimate the total coverage of adhesion components, we compared the positively identified proteins within our datasets against the consensus adhesome, which was based on IAC enrichment approaches in 2D fibronectin substrates.⁴⁷ The BioID2-paxillin dataset generated here achieved identification of 80% of the paxillin-FAK axis, as well as 75% of the talintinculin axis (Figure S1F). Two additional consensus adhesome proteins were identified in the talin1-13x-BioID2 dataset (testin and zyxin) that were not identified in the BioID2-paxillin dataset. Both of these proteins form part of the actinin-zyxin module.

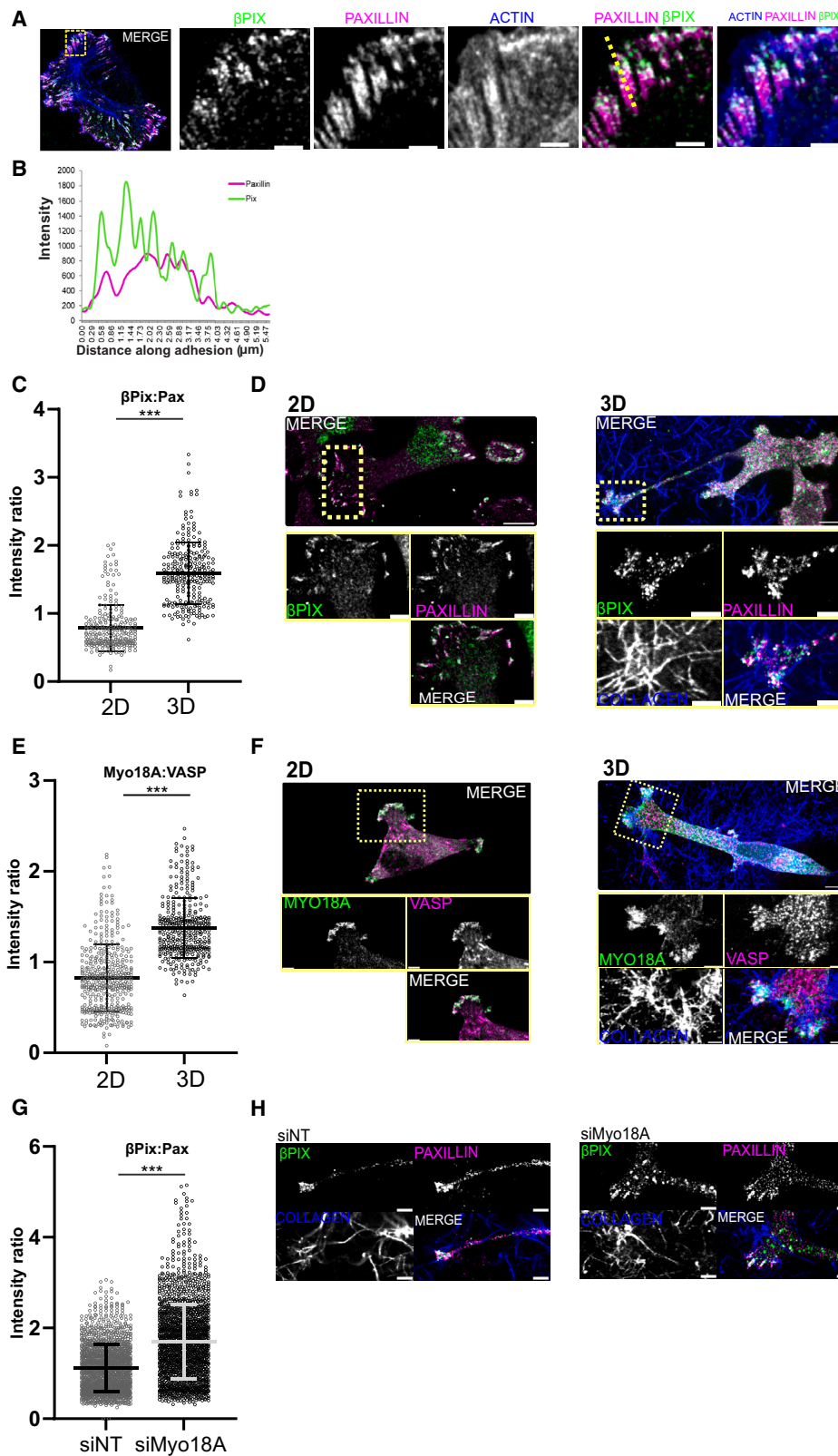
Myosin-18A and Git1/ β Pix are enriched in 3D adhesion sites

Having identified proteins exhibiting differential proximity on 2D or in 3D substrates, we next sought to identify candidate regula-

tory proteins recruited to adhesions in 3D matrix. To achieve this, we focused on the BioID2-paxillin dataset, because paxillin is located within the adhesion signaling layer of IACs,⁹ and interrogated the datasets to identify subnetworks of known interactors, each exhibiting a similar enrichment profile toward BioID2-paxillin in 3D ECM. ARHGEF7 (also known as β Pix), Git1, and Git2 were found to be enriched within 3D matrices in the BioID2-paxillin dataset (Figure 1D), whereas their overall expression was unchanged (Figures S1G and S1H). β Pix and the Git proteins are known to form a complex and are established IAC components in cells cultured on 2D substrates.^{5,50} β Pix is also upregulated in breast cancer⁵¹; thus, we chose to investigate the role of β Pix in 3D embedded cells. To do so, an initial preliminary BioID2- β Pix screen in MDA-MB-231 cells was conducted comparing the interactors of β Pix in 2D versus 3D environments (Figure 1F). This screen identified several proteins that β Pix is known to bind: Git1/2, SCRIB, and Myo18A.^{52,53} Of these, only Myo18A was found exclusively in the 3D matrices compared to the 2D substrate (Figure 1F). These data suggested a putative role for the β Pix/Myo18A complex in 3D microenvironments. Thus, we sought to investigate the potential role of β Pix/Myo18A in 3D invasive cell migration.

Initially, β Pix and Myo18A localization in cells plated on 2D substrates was examined. In these conditions, β Pix clearly localized at paxillin-positive adhesion sites, where β Pix shows enrichment at the membrane-proximal region of adhesion complexes (Figures 2A, 2B and S2A). We examined Myo18A localization through GFP-Myo18A expression with mCherry-Vinculin (Figure S2B). We observed the accumulation of GFP-Myo18A in adhesions on 2D substrates, yet with a more dispersed pattern compared with β Pix localization. Together, these data suggest that both β Pix and Myo18A can localize at, or in close proximity to, adhesions in MDA-MB-231 cells plated on 2D matrices, as previously reported for β Pix in other cell types.^{5,54}

Having confirmed β Pix and Myo18A localization on 2D substrates, we next examined this in cells embedded in 3D matrices. Endogenous β Pix and Myo18A both showed enrichment at paxillin-, VASP-, and vinculin-positive adhesion structures, which were coincident with collagen fibers (Figures 2C–2F, S3A, and S3B). Quantification of β Pix/Myo18A versus their respective adhesion partners showed that their enrichment is higher in 3D matrices versus 2D surfaces (Figures 2C and 2E), confirming the MS results. These results established that β Pix and Myo18A are both enriched at adhesive sites in 3D embedded cells. It is known that β Pix accumulation is negatively regulated through actomyosin contractility,⁵ which we confirm here with an increase in β Pix localization at adhesions following blebbistatin treatment on 2D surfaces (Figures S2C–S2G). Because Myo18A binds to β Pix as well as NM2,^{49,51} we proposed that Myo18A depletion may also have an effect similar to that of NM2 inhibition. Myo18A-depleted cells revealed an increase in β Pix intensity at adhesions, similar to blebbistatin treatment, with a reduction in paxillin intensity (Figures S2C–S2I). These results were observed in both 2D and 3D environments for β Pix intensity relative to the adhesion marker (Figures 2G and 2H). Myo18A depletion also altered β Pix distribution from enrichment at the membrane-proximal region of adhesions to a more even distribution along the length of adhesions (Figure S2I).



(legend on next page)

β Pix is thought to reside in a complex with Git1.⁵⁰ Similar to β Pix, Git1 localization at adhesions increased when we depleted Myo18A or inhibited NM2 (Figures S2J–S2L). This suggests that Git1/ β Pix are removed from adhesions by a force-dependent mechanism. Git1/ β Pix recruitment to adhesions is enabled through Git1 binding to the LD2 and LD4 domains of paxillin.⁵⁵ Git1 binds paxillin through its C-terminally located paxillin-binding region, a structured 4-helix bundle (called here GPBR).⁵⁶ Therefore, we examined whether the GPBR alone responds to Myo18A depletion or NM2 inhibition like full-length Git1/ β Pix. GFP-GPBR was expressed in cells depleted of Myo18A or subjected to blebbistatin treatment. GPBR intensity in adhesions was measured in comparison to paxillin (expressed as mApple-paxillin). Similar to full-length GIT1, GPBR levels in adhesions were also increased in Myo18A-depleted or blebbistatin-treated cells (Figures S2M and S2N). This reveals a previously unknown force-modulated binding to the paxillin LD2–LD4 domain that negatively regulates Git1/ β Pix retention in adhesions.

β Pix and Myo18A are required for invasive migration

Having identified that β Pix and Myo18A associate with adhesions in 3D matrices, we examined what role they may play in cell invasion. The ability of MDA-MB-231 cells to invade extracellular matrices was examined using inverted invasion assays. Cells were embedded in Matrigel supplemented with fibronectin and examined for their ability to invade into matrices. Depletion of either β Pix or Myo18A by small interfering RNA (siRNA) (Figure S3C) resulted in a significant decrease in invasion similar to the levels achieved with metalloproteinase inhibitor GM6001 treatment (Figures 3A and 3B).

Effective invasive cell migration through restrictive matrices requires the ability to remodel and degrade the surrounding matrix.^{1,33} To measure the ability of MDA-MB-231 cells, depleted of β Pix or Myo18A, to degrade matrices, we examined invadopodial formation and collagen degradation ability. Loss of β Pix or Myo18A caused no decrease in the amount of degradation, measured by the percentage of cells associated with degradation spots, as well as degraded patches per cell (Figures S3E–S3G). Loss of β Pix or Myo18A expression did not cause a

change in 3D collagen matrix degradation, measured by change in fluorescence of DQ collagen spiked collagen gels (fluorescence increases with collagen degradation; Figures S3H and S3I). Together, these results suggest that while β Pix or Myo18A regulate invasive cell migration, there is no defect in the ability of β Pix- or Myo18A-depleted cells to degrade extracellular matrices.

To examine the effect of siRNA-mediated β Pix or Myo18A suppression on cell migration in 3D matrix, we performed single-cell tracking during invasion. Cells depleted of β Pix or Myo18A were reduced in their ability to migrate in the matrix environment (Figures 3C and 3D; Videos S1, S2, and S3). Wound healing assays with cells plated on fibronectin/collagen-coated plastic showed comparable results; depletion of either β Pix or Myo18A led to a reduction in wound closure over 40h by 48% and 78%, respectively, compared to control cells (Figure S3D). Effective cell migration requires precise coordination of adhesion dynamics, and β Pix has previously been reported to negatively regulate adhesion maturation and promote nascent adhesion turnover.⁵ Therefore, we examined the effect of β Pix or Myo18A depletion on matrix adhesions in MDA-MB-231 cells. We observed an increase in the number of small adhesions ($\leq 2 \mu\text{m}^2$) on 2D substrates and on pseudopods in 3D matrix, as well as an increase in the number of adhesions per cell on 2D surfaces (Figures S3J–S3L).

Together, these results suggest that β Pix and Myo18A are required for efficient migration. Adhesions are still assembled in β Pix- and Myo18A-depleted cells but differ in size and number from their wild-type counterparts. In 3D, β Pix or Myo18A depletion does not negatively affect matrix degradation, yet it does inhibit invasive migration, suggesting a direct impact on cell motility.

β Pix and Myo18A regulate nuclear morphology and internal cell polarity

To further investigate the cause of the migration and invasion defects seen with β Pix or Myo18A depletion, we examined further parameters related to cell migration. MDA-MB-231 cells form characteristic pseudopodia during 3D cell invasion,¹⁴ a process

Figure 2. β Pix and Myo18A enrich in 3D adhesive sites

(A) Representative images of MDA-MB-231 cells fixed and stained for phalloidin (blue), Paxillin (magenta), and β Pix (green). Boxed region indicates region of magnified view (bottom). Images are single z slice projections. Scale bar in expanded view, 10 μm ; in magnified view, 2 μm .

(B) Line scan profile of Paxillin and β Pix across focal adhesion shown in (A) with dashed line. Magenta line indicates Paxillin intensity; green line indicates β Pix intensity.

(C) Ratio of fluorescence intensity of β Pix/Paxillin in MDA-MB-231 cells plated on glass coverslips (2D) or embedded in collagen (supplemented with $\sim 1\%$ – 2% fluorescent collagen [blue] and fibronectin) gel (3D). Two-sample t test was used to estimate p value. ***p < 0.001. N = 4 independent experiments; n = 16–18 cells, n = 283–315 adhesions.

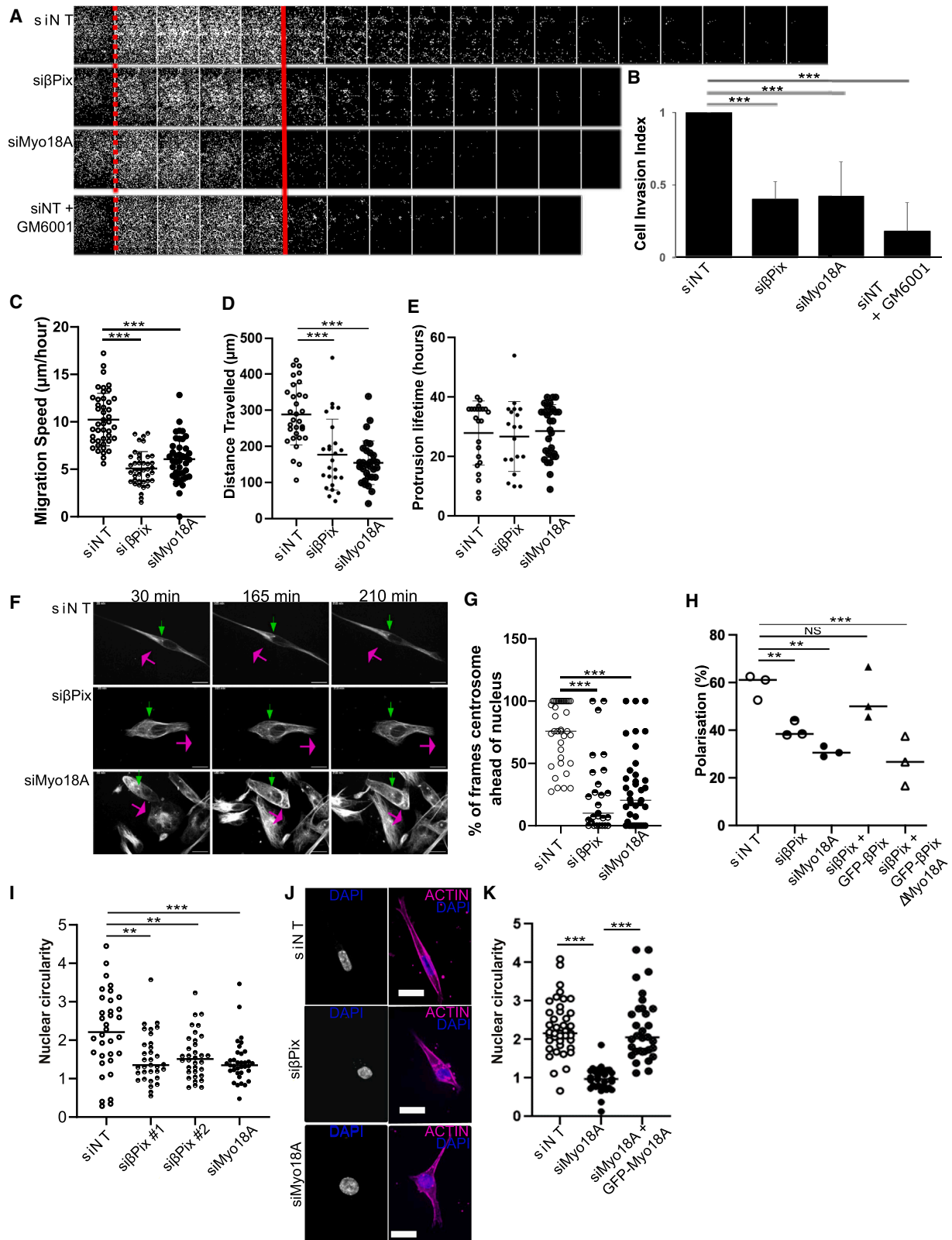
(D) Representative images of MDA-MB-231 cells plated on glass coverslips (2D) or in collagen/fibronectin gel. Cells are stained for Paxillin (magenta), β Pix (green), and collagen (blue) where included. Scale bar in expanded view, 10 μm ; in magnified view, 5 μm . Rotated 90° clockwise in 2D inset.

(E) Ratio of fluorescence intensity of Myo18A/VASP in MDA-MB-231 cells plated on glass coverslips (2D) or embedded in collagen (supplemented with $\sim 1\%$ – 2% fluorescent collagen [blue] and fibronectin) gel (3D). N = 4 independent experiments; n = 14–18 cells, n = 395–414 adhesions. Two-sample t test was used to estimate p value. ***p < 0.001.

(F) Representative images of MDA-MB-231 cells plated on glass coverslips (2D) or collagen/fibronectin gel. Cells are stained for VASP (magenta), Myo18A (green), and collagen (blue) where included. Scale bar in expanded view, 10 μm ; in magnified view, 5 μm . Rotated 180° in inset.

(G) Ratio of fluorescence intensity of β Pix/Paxillin MDA-MB-231 cells treated with siNT or Myo18A-siRNA. Cells embedded in collagen (supplemented with $\sim 1\%$ – 2% fluorescent collagen [blue] and fibronectin) gel, N = 4 independent experiments; n = 35 cells, n = 1700–1800 adhesions. Two-sample t test was used to estimate p value. ***p < 0.001.

(H) Representative images of MDA-MB-231 cells treated with NT or Myo18A-siRNA embedded in collagen/fibronectin gel. Cells are stained for Paxillin (magenta), β Pix (green), and collagen (blue). Scale bar, 5 μm .



(legend on next page)

that is highly dependent upon actin dynamics. Therefore, the ability of β Pix- or Myo18A-depleted cells to assemble actin protrusions in 3D matrices was examined. Following β Pix or Myo18A depletion, no defect in actin protrusion length or lifetime was observed (Figures 3E, S4A, and S4B), suggesting that the invasion defect is not due to a defect in global actin assembly parameters.

β Pix has been reported to exhibit GEF activity for CDC42 and Rac *in vitro*⁵⁷; however, this activity is not consistently observed in cells.^{22,58} We therefore chose to examine the global activity of the Rho guanosine triphosphatases (GTPases) Rac1 and CDC42 following β Pix depletion using 2 separate approaches: Förster resonance energy transfer (FRET)/fluorescence lifetime imaging microscopy of live cells expressing Rac1 or Cdc42 FRET biosensors,^{59,60} and PAK-PBD pull-down assays to measure Rac1 and Cdc42 activity. No change in Rac1 or Cdc42 activity was observed in β Pix-depleted cells in either assay (Figures S4G and S4H).

A reduction in actomyosin contractility could also be a cause of defective migration.⁶¹ However, the depletion of β Pix did not show a reduction in myosin light chain (MLC) phosphorylation (Figures S4I and S4J). In addition, RNA-seq and western blot analysis suggest that the expression levels of NM2A/B heavy chain are unaltered following β Pix/Myo18A depletion (Figures S5A and S5B). These data, together with the ability to form pseudopodial protrusions, suggest that the observed migration defects in response to β Pix depletion are not a consequence of disruption to Rac and CDC42 signaling or levels of active NM2A/B expression.

Established front-rear cell polarity is required for cell migration.⁶² We qualitatively observed rounded, well-spread cells that lacked a clear front and rear following β Pix/Myo18A depletion on 2D surfaces and chose to further investigate cell polarity. Using the centrosome as an indicator of cell polarity,⁶³ we visu-

alized migrating cells in 3D matrices in long-term time lapses to measure their polarization, as previously described.⁶⁴ Cells were scored as polarized when the centrosome was in front of the nucleus or as unpolarized when the centrosome was to the rear of the nucleus, relative to the direction of migration (Figure S5C). Non-Targeting siRNA (siNT)-treated cells showed 74% centrosome polarity, whereas depletion of either β Pix or Myo18A reduced polarization drastically to 25% and 28%, respectively (Figures 3F and 3G; Videos S4, S5, and S6).

To verify these results in a controlled environment, we examined cells plated on crossbow-shaped Cytoo coverslips. Cells were scored as polarized if the microtubule-organizing center (MTOC) centrosome was located in the front third of the cell (from the center of the nucleus; Figure S5D). Using this method, 59% of control cells show polarization, whereas the depletion of β Pix or Myo18A caused a significant reduction in polarization, with only 40% and 31%, respectively, of cells polarized (Figures 3H and S5E). Having identified a role for β Pix and Myo18A in internal cell polarity, we postulated that this may be via the ability of β Pix to bind Myo18A. To test this, we undertook rescue experiments of β Pix-depleted cells with either full-length β Pix (GFP- β Pix) or a truncated β Pix construct, which lacks the C-terminal PAWDLTL motif that is required for Myo18A binding (GFP- β Pix Δ Myo18A).⁵² Although GFP- β Pix expression in β Pix-depleted cells was able to rescue cell polarization, the expression of GFP- β Pix Δ Myo18A did not rescue the polarization defect (Figures 3H and S5E), demonstrating the requirement for β Pix/Myo18A binding in cell polarization.

Another factor required for efficient migration is correct nuclear morphology and positioning^{36,40,41,42}; therefore, the nuclei morphology of cells depleted of β Pix or Myo18A was examined in cells embedded in 3D ECM. Unlike their wild-type counterparts, which often contained elongated nuclei, oriented along the axis of the pseudopods, β Pix or Myo18A depletion led to a

Figure 3. β Pix and Myo18A localize to 3D adhesive sites and are required for cell invasion and polarity

- (A) Inverted transwell invasion assay. MDA-MB-231 cells treated with siNT, β Pix-siRNA, or Myo18A-siRNA or GM6001 (MT1-MMP inhibitor). Cells were subjected to inverted invasion assay in Matrigel/fibronectin gels for 5 days. Cells were fixed and stained with Hoechst. Images were taken every 10 μ m into gel.
- (B) Data represent cell invasion index: fold change in percentage of cells invading ≥ 40 μ m depth (red solid line)/N = ≥ 4 experiments. One-way ANOVA; Dunnett's multiple comparison post-test versus siNT to estimate p values. *p < 0.05; ***p < 0.001. Error bars are SDs.
- (C–E) Circular invasion assay (CIA). (C) Single-cell migration speed. MDA-MB-231 cells treated with siNT, β Pix-siRNA, or Myo18A-siRNA. Cells were examined for migration speed. One-way ANOVA; Dunnett's multiple comparison posttest versus siNT to estimate p values. ***p < 0.001. Data represent n = 40–41 cells per condition, N = 4 independent experiments. (D) Single-cell distance traveled in CIA. One-way ANOVA; Dunnett's multiple comparison posttest versus siNT to estimate p values. ***p < 0.001. (E) Single-cell protrusion lifetime in CIA. Data represent n = 33–35 cells per condition, N = 3 independent experiments. Cells were subjected to CIA for 24–48 h.
- (F) Representative images of MDA-MB-231 cells stained with SiR-tubulin embedded in collagen/fibronectin gels, treated with siNT, β Pix-siRNA, or Myo18A-siRNA. Three time-lapse stills shown for each condition. Green arrow indicates centrosome location. Magenta arrow indicates cell migration direction. Scale bars, 10 μ m.
- (G) Dot plot shows the percentage of time points that cells were polarized based on centrosome location relative to nucleus during migration (analysis as illustrated in Figure S5C). Cells were considered to be polarized if the centrosome was located in the front third of the cell and in front of the nucleus during migration. Cells were considered to be unpolarized if the centrosome was in the back two-thirds of the cell. N = 3 independent experiments; n = 27–39 cells. One-way ANOVA; Dunnett's multiple comparison posttest versus siNT to estimate p values. ***p < 0.001.
- (H) Polarization of cells on CYTOO crossbow chips, as illustrated and outlined in Figures S5D and S5E. N = 3 independent experiments; n = 9–51 cells. Error bars: SEMs. One-way ANOVA; Dunnett's multiple comparison posttest versus siNT to estimate p values. **p < 0.01; ***p < 0.001; NS, non-significant.
- (I) Nuclear circularity ratio (long/short length) of NT, β Pix, or Myo18A siRNA-treated cells. One-way ANOVA; Dunnett's multiple comparison posttest versus siNT to calculate p values. **p < 0.01; ***p < 0.001. Data represent n = 33–35 cells per condition, N = 3 independent experiments.
- (J) Representative images of MDA-MB-231 cells treated with siNT, β Pix-siRNA, or Myo18A-siRNA, stained with SiR-Actin (magenta) and Hoechst (blue). Scale bars, 20 μ m. MDA-MB-231 cells were embedded in collagen (supplemented with \sim 1%–2% fluorescent collagen and fibronectin) gel.
- (K) Nuclear circularity ratio (long/short length) of NT- or Myo18A siRNA-treated cells \pm GFP-Myo18A. MDA-MB-231 cells were embedded in collagen (supplemented with \sim 1%–2% fluorescent collagen and fibronectin) gel. One-way ANOVA; Dunnett's multiple comparison posttest versus siNT to estimate p values. ***p < 0.001. Data represent n = 30–41 cells per condition, N = 3 independent experiments.

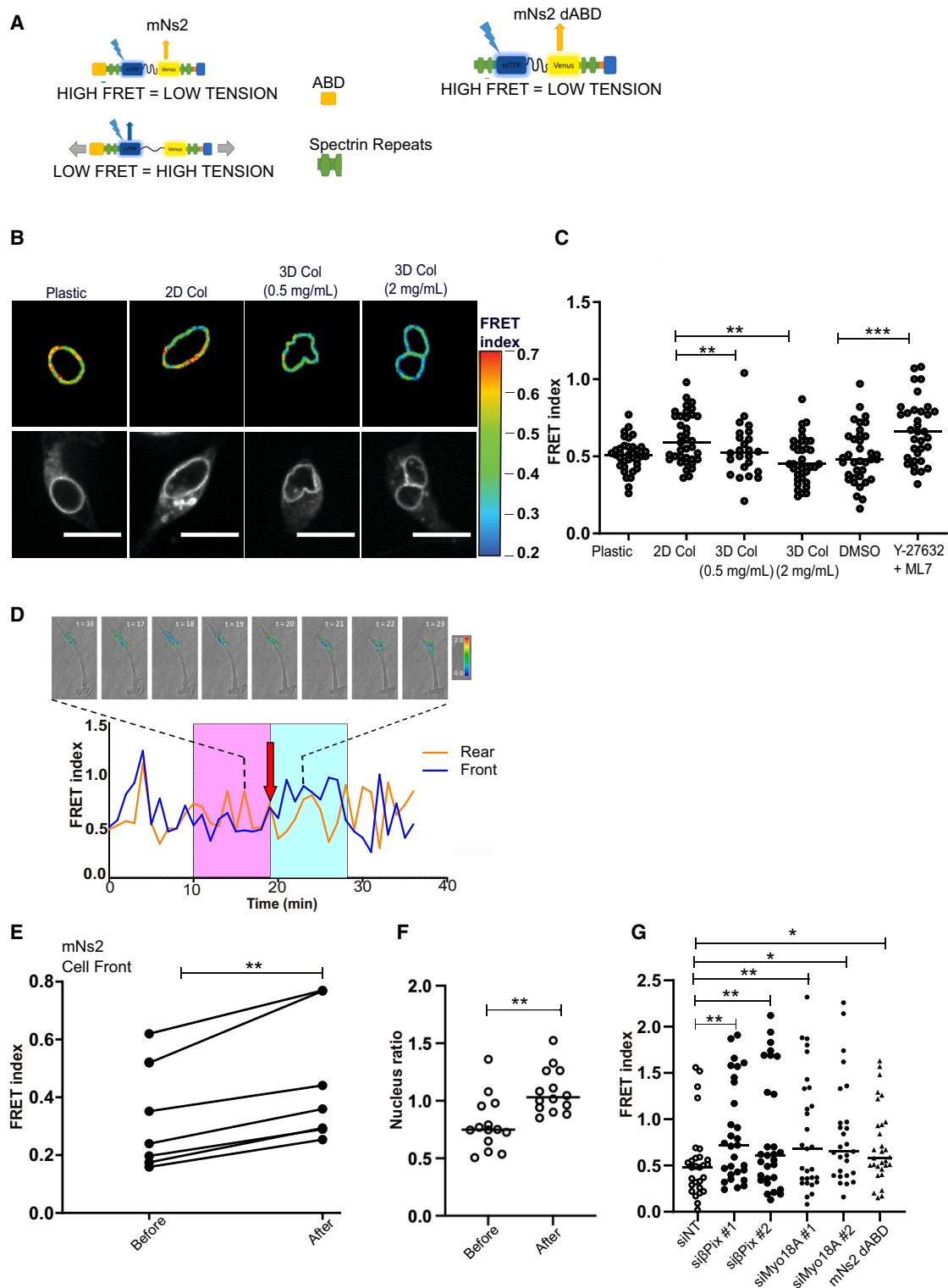


Figure 4. β Pix and Myo18A are required for nuclear force transmission

(A) Schematic of FRET sensors: low FRET equates to high tension and high FRET indicates low tension. mNs2 and mNs2-dABD. MNs2-dABD lacks actin-binding calponin homology domain (ABD) domain at the N terminus of protein.

(legend continued on next page)

higher degree of nuclear roundness, and the nuclei were not oriented in the direction of the associated pseudopod, an effect that could be rescued by the reexpression of EGFP-Myo18A in Myo18A-depleted cells (Figures 3I–3K).

In conclusion, these data show that the reduction in 3D cell migration following β Pix or Myo18A depletion is not due to a defect in matrix degradation, protrusion formation, or altered Rho GTPase signaling. Rather, the functional β Pix/Myo18A module is required for invasion/migration, nuclear shape adaptation, and maintenance of front-rear polarity.

β Pix and Myo18A are required for nuclear force transmission

Nesprins are nuclear-associated LINC complex members, which have been shown to be required for front-rear cell polarity and cell migration in constricted 3D environments.^{36,63} The nucleus is the major obstacle to invasive cell migration in matrices with pore sizes resembling the *in vivo* ECM³³ and is under actomyosin-mediated tension.^{41,65} We therefore hypothesized that β Pix/Myo18A could affect actomyosin-dependent nuclear force coupling, leading to defective nuclear translocation and invasion.

We examined whether the nucleus is under a different amount of tension when found in 3D compared to 2D environments. To examine this, we used a mini-nesprin-2 FRET-based biosensor (mNs2).⁶⁵ Here, a higher FRET readout indicates the nuclear region is under low tension, whereas a lower FRET readout indicates higher tension (Figure 4A). Using this approach, we found MDA-MB-231 cells embedded in 3D matrices in concentrations that are permissive (0.5 mg/ml collagen) and restrictive (2 mg/ml collagen) to migration were under greater tension, compared to cells plated on a 2D surface with matrix coating (Figures 4B and 4C). Confirming the role of actomyosin contractility, cells embedded within the 2 mg/mL matrix were treated with 20 μ M Y-27632 and ML-7 (a Rho kinase inhibitor and an MLC kinase inhibitor, respectively). Inhibitor treatment significantly reduced the tension across the mini-nesprin2 tension sensor, with the FRET index returning to levels seen in cells in 2D substrates (Figure 4B and 4C).

Next, we examined nuclear tension during restrictive 3D cell migration (cells embedded in 2 mg/mL gels). The nuclear tension of migrating MDA-MB-231 cells expressing the mini-nesprin-2 FRET tension sensor or mini-nesprin-2 FRET tension sensor

lacking the nesprin2 actin-binding domain (called mNs2-dABD; Figure 4A) was tracked over 40 min. Under these conditions, our measurements show that the nucleus is under greater tension (lower FRET readout) in the front half of the nucleus before cell and nuclei movement occurs and a substantial decrease in tension is observed following nuclear translocation through an ECM pore (Figures 4D and 4E). This was not observed in the rear of the nucleus or with the nesprin tension sensor lacking the actin-binding domain (Figure S6). The changes in tension observed on the FRET sensor were accompanied by a change in nuclear shape, and the front of the nucleus is narrower in diameter compared to the rear of the nucleus before cell and nucleus migration; this narrowing is lost at the point following nuclear translocation (Figure 4F).

Having identified that there is an increase in nuclear tension in the front half of the nucleus before cell migration and an alteration to nuclear morphology following β Pix and Myo18A loss, we examined whether β Pix or Myo18A are required for nuclear force transmission. β Pix- and Myo18A-depleted cells were transfected with the tension sensor and embedded in 3D environments and imaged by live-cell microscopy. Depletion of either β Pix or Myo18A resulted in a significant increase in FRET index across the nucleus (Figure 4G). A similar increase in FRET, indicating a decrease in tension, was observed following the expression of mNs2-dABD (Figure 4G).^{66,67}

Together, these data show that force is actively applied to the front region of the nucleus during 3D cell migration and that β Pix and Myo18A are required for effective mechanotransduction from IACs to the nucleus in cells migrating through matrices.

β Pix/Myo18A generates a NM2A/B gradient required for cytoskeletal-nuclear force coupling

Myo18A is known to coassemble with NM2,⁶⁸ and NM2 isoform polarization is required for front-rear cell polarity.^{31,69} Therefore, we investigated whether the β Pix/Myo18A module at adhesion sites is required for NM2 isoform-mediated front-rear cell polarity and migration.

A CRISPR knockin MDA-MB-231 cell line expressing mNeon-NM2A (called 231-mNeonNM2A hereafter) was created to ensure endogenous levels of NM2A during live-cell analysis. Preliminary examination of 231-mNeonNM2A cells embedded in 3D matrices revealed a strong accumulation of NM2A at newly forming adhesion sites preceding paxillin recruitment (Figures 5A and

(B) Confocal imaging of MDA-MB-231 cells expressing the mNs2 tension sensor in 2D (plastic or plastic coated with collagen) and 3D environments (0.5 or 2 mg/ml). Pseudocolored to represent FRET index (scale on right side).

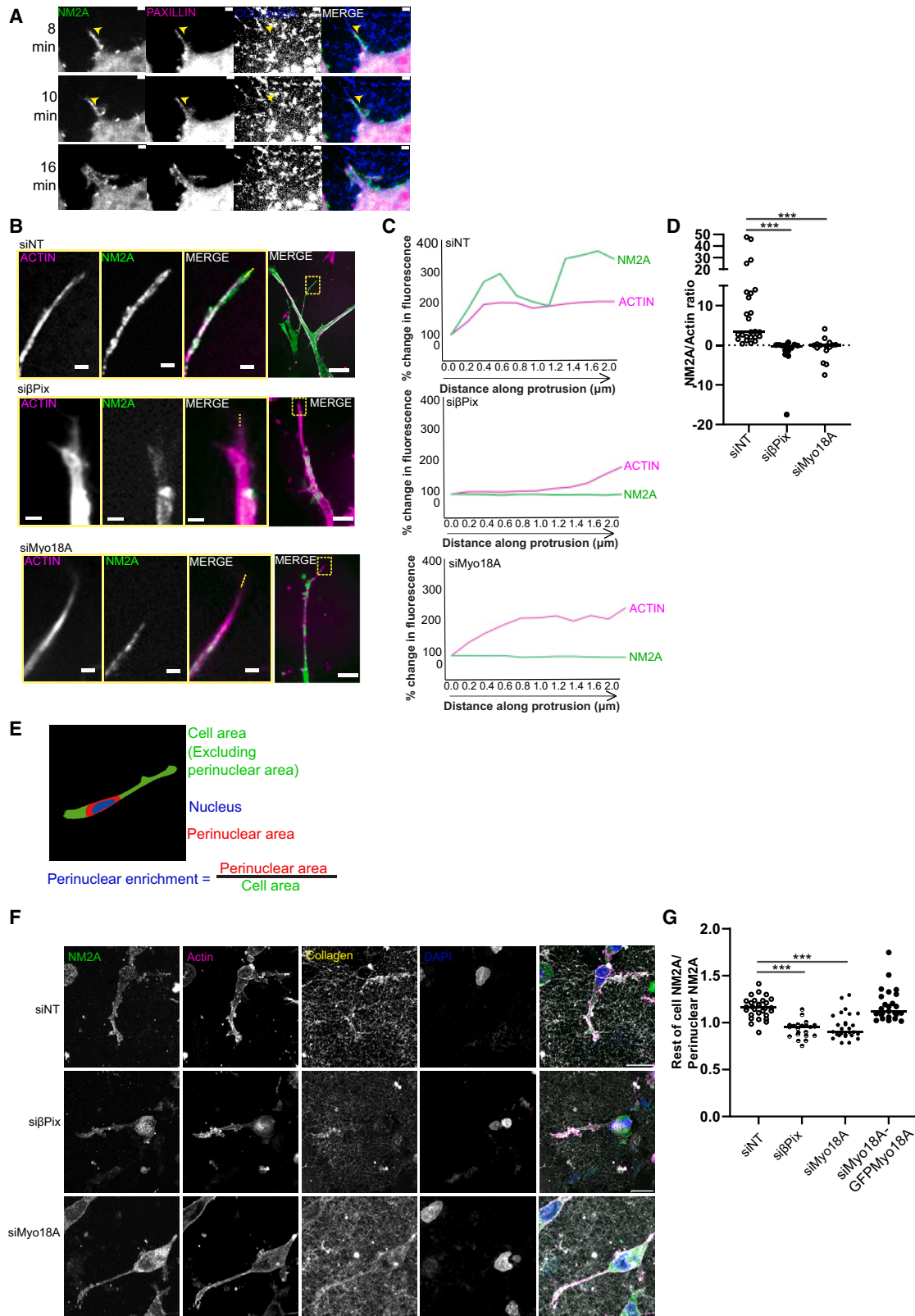
(C) The average FRET index across a central cross-section of the nuclear envelope (in the horizontal plane) of MDA-MB-231 cells. Drug treatment used 20 μ M Y-27632/ML-7 and was compared to cells treated with an equivalent volume of DMSO. N = 4 experiments, SEM. **p < 0.01; *** p < 0.001.

(D) Trace of FRET index measured for the front and rear halves of the nucleus in 2 mg/mL gel. MDA-MB-231 cells expressing mN2-TS images showing FRET ratio (pseudocolored) overlaid onto bright-field images. Images correlate to the time point range highlighted (dotted lines). Red arrow on timescale indicates moment of nuclear translocation. FRET index for the 10 time points before nuclear movement (pink box in C) was shown to be significantly lower than the 10 time points after the initiation of movement (blue box in C) (p = 0.067, paired t test).

(E) Average FRET index of the front face of the nucleus before (pink box in C) and after translocation (blue box in C) for 7 cells as imaged in (C). p = 0.0133, paired t test. N = 4 experiments. **p < 0.01.

(F) Dot plot of nucleus ratio front/rear from MDA-MB231 cells before (pink box in C) and after translocation (blue box in C) in collagen/fibronectin gel. Two-sample t test was used to estimate p values. **p < 0.01. Data represent n = 14 cells, N = 3 independent experiments.

(G) FRET index of MDA-MB-231 cells embedded in collagen/fibronectin gel. Gel treated with siNT, β Pix-, or Myo18A-siRNA or transfected with Nesprin-tension sensor lacking N-terminal actin-binding domain (mN2-TS dABD). One-way ANOVA; Dunnett's multiple comparison posttest versus siNT to estimate p values. *p < 0.05; **p < 0.01. N = 3 experiments, n = 27 cells.



(legend on next page)

S7A; Video S7). We transfected 231-mNeonNM2A cells with mApple-Paxillin to study live-cell dynamics in 3D matrices. NM2A is recruited to and enriched in adhesive sites, which also appear to resemble the sites for new protrusion assembly (Figure 5A; Video S7). More importantly, this contrasts with the distribution of NM2A in cells plated on a 2D surface, where we and others⁷⁰ have observed less clear enrichment of NM2A at adhesive sites (Figure S7B).

The effect of β Pix and Myo18A depletion on NM2A localization was examined using the 231-mNeonNM2A in 3D matrices. Cells were stained with SiR-Actin to mark actin-based protrusions and imaged by live-cell microscopy. We observed no change in overall NM2A or actin intensity in the pseudopodia of β Pix-depleted cells compared to controls (Figures S7C–S7E). However, the characteristic enrichment of NM2A fluorescence intensity toward the distal tip of actin protrusions ($\sim 2 \mu\text{m}$ along the length of the protrusion, toward the cell body) was absent in the β Pix/Myo18A-depleted cells (Figures 5B–5D). When examining cells on a 2D surface, the depletion of β Pix or Myo18A reduced the average intensity of NM2A staining that is in close proximity to a paxillin-based adhesion mask (Figures S7F–S7H).

NM2A and NM2B form a gradient within cells plated on 2D surfaces and in 3D matrices.^{32,36} We verified these findings using MDA-MB-231 cells stained for NM2A and NM2B in 3D matrices, where NM2B accumulates in the perinuclear region and NM2A is distributed throughout the cell, with prominent staining in pseudopodial tip regions (Figures 5F, 6A, and S7A). Remarkably, depletion of either β Pix or Myo18A causes a loss of the NM2A/NM2B polarization within cells, with NM2A being no longer enriched at pseudopod tips or in the cell periphery (Figures 5B–5G) and NM2B being less enriched in the perinuclear region and distributed throughout the cytoplasm (Figures 6A–6C). This effect could be rescued by the expression of GFP-Myo18a in Myo18A-depleted cells (Figures 5F, 5G, S7J, and S7K).

Having determined that the expression of the mNs2-dABD tension sensor does not show significant force applied on the sensor (Figure 4), and knowing nesprin-2 is required for 3D cell migration,³⁶ we examined the effect of a dominant-negative KASH domain-only nesprin construct (DN-Nesprin) on NM2B polarity. DN-Nesprin expression in MDA-MB-231 cells causes a loss of NM2B polarization (Figures 6D and 6E), similar to β Pix/Myo18A depletion.

Together, these data show that β Pix/Myo18A are required for the efficient recruitment of NM2A to adhesion sites and essential for the polarized distribution of NM2A-NM2B needed for cell migration and invasion (Figure 6F). This demonstrates that migrating cells establish a connected network of actomyosin-mediated force coupling from adhesion sites in protrusions to the nucleus, which underpins successful 3D invasive cell migration.

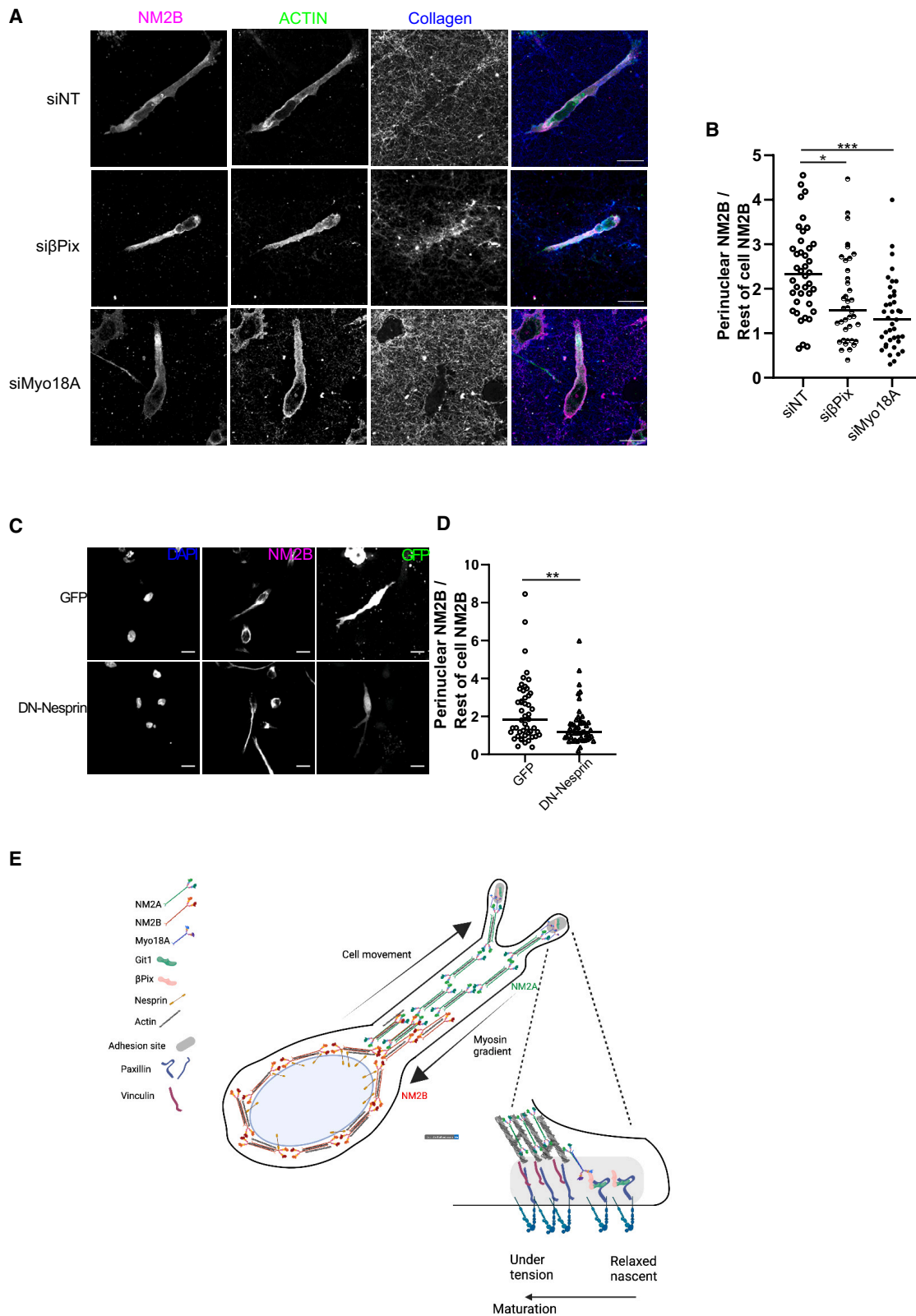
DISCUSSION

This study identifies the composition of core components of cell matrix adhesion sites in cells migrating within 3D matrices. Differences in the composition between adhesion complexes on stiff 2D and soft 3D matrices reveal the establishment of polarity in the actomyosin network as a function of maturation of adhesion sites in 3D matrices, which is required for invasive migration. The 3D matrix adhesion sites are relatively enriched in β Pix and Myo18A, two proteins that are needed for initial NM2A recruitment to adhesion sites in protrusions and NM2A/NM2B isoform gradient formation across the cell. Cells moving through 3D matrices actively translocate their nucleus. Here, we show dynamic nuclear force transduction between adhesion sites and the LINC complex in the nuclear membrane during 3D invasive cell migration. Loss of actomyosin connectivity at adhesion sites or the nucleus leads to a loss of nuclear force coupling and a failure to establish the NM2 isoform polarity gradient. We propose a model whereby mechanical coupling between IACs and the nucleus is required for the formation of an NM2A/NM2B gradient; the gradient in turn is essential to couple nuclear movement to cell migration (Figure 6F). We show that nuclear actomyosin force coupling from adhesion sites in 3D matrices is an essential requirement for invasive cancer cell migration.

To the best of our knowledge, this work represents the first systemic analysis of the adhesion proteins were identified here (Figure 1; Data S1–S3), as well as a significant proportion of established consensus adhesion components in IACs from both 2D and 3D environments.^{47,71} Results of the 2D IAC experiments also compared well with previously published BiolD screens of paxillin.^{7,72} This suggests that the core adhesion machinery and architecture remain conserved in a 3D microenvironment. The compositional changes observed in cells in a 3D matrix, compared with 2D, are highly reminiscent of those found when

Figure 5. β Pix and Myo18A are required for NM2A recruitment to protrusive tips

- (A) MDA-MB-231 cells expressing NM2A-mNeon (green) transfected with mApple-Paxillin (magenta) embedded in collagen (supplemented with $\sim 1\%$ – 2% fluorescent collagen [blue] and fibronectin). Gels were imaged by live-cell microscopy. Protrusive structures are indicated with yellow arrowhead.
- (B) Representative images of MDA-MB-231 cells expressing NM2A-mNeon (green) treated with siNT, β Pix-siRNA, or Myo18A-siRNA embedded in collagen/fibronectin gels. Cells stained with SiR-Actin (magenta). Images on the left are expanded views, yellow-boxed regions indicate zoom region shown on the right. Scale bar expanded, $10 \mu\text{m}$; magnification, $2 \mu\text{m}$.
- (C) Percentage change in fluorescence signal along actin protrusion, starting at most distal point. Example fluorescence line scans of actin/NM2A from enlarged images indicated by yellow dashed line shown in (B).
- (D) Fluorescence intensity ratio of NM2A/actin signal at $2 \mu\text{m}$ point from tip of protrusion. $n = 16$ – 26 cells, $N = 3$ independent experiments. One-way ANOVA; Dunnett's multiple comparison post-test versus siNT to calculate p values. *** $p < 0.001$.
- (E) Schematic to show quantification method for data shown in (G).
- (F) Representative images of MDA-MB-231 cells treated with siNT, β Pix-siRNA, or Myo18A-siRNA embedded in collagen/fibronectin gels stained for DAPI (blue), NM2A (green), and actin (magenta). Scale bars, $20 \mu\text{m}$.
- (G) Graph shows ratio of cellular NM2A intensity and perinuclear NM2A intensity (quantified as in E). One-way ANOVA; Dunnett's multiple comparison post-test versus siNT to estimate p values. *** $p < 0.001$. Data represents $n = 23$ – 34 cells per condition, $N = 3$ independent experiments.



(legend on next page)

cellular contractility is inhibited by blebbistatin treatment, with reduced enrichment of mechanosensitive LIM domain-containing proteins and enhanced recruitment of the Git- β Pix complex.^{5,6}

Our study has identified factors required for the invasive migration of breast cancer cells in 3D environments. Of the proteins enriched in 3D adhesion sites, β Pix, Git1/2, and Myo18A stood out as previously identified IAC components with unknown roles in cancer cell invasion. We show that β Pix and Myo18A are essential for invasion and 3D migration without affecting the ability of cells to degrade matrix, form pseudopods, or reduce global Rac and CDC42 activity. The latter was perhaps unexpected because β Pix has previously been associated with GEF activity in fibroblasts and contains a Dbl homology (DH) domain.^{57,73} However, more recent publications have shown minimal GEF activity for β Pix,²² and early structural studies revealed that the β Pix DH domain has mutations in key residues that preclude activity.⁵⁸ With these previous publications and the data presented here, we propose that the lack of migration and invasion is not caused by changes in actin polymerization in β Pix- or Myo18A-depleted cells. We were, however, able to confirm a previously observed cell shape change following the depletion of β Pix/Myo18A.⁷⁴ Cells were visibly more circular and spread than their wild-type counterparts, with an inability of the cells to polarize their MTOC on defined micropatterns. This phenotype was reminiscent of cells having defects in connections of the cytoskeleton to the nucleus.³⁶

Actomyosin-mediated tension can be sensed by the nucleus, in particular in 3D matrix environments.^{41,65,75} Nuclear force transduction has been postulated to play an important role in cell migration,³⁴ but measurements of the forces applied on the nucleus during 3D invasive cell migration have not previously been documented. Here, we show that cancer cells invading 3D collagen gels actively apply forces on the nucleus. When movement of the nucleus is stalled, despite continued protrusion formation—presumably due to the cell encountering an obstacle—tension at the front of the nucleus increases before nuclear movement. Following forward translocation, as the nucleus moves past the obstacle, a noticeable drop in tension at the front of the nucleus is observed. The results here suggest that the nucleus in 3D matrix is, at least in part, pulled forward by actomy-

osin forces applied to the nucleus via nesprin. This idea is strengthened by studies demonstrating the accumulation of specific nesprins at the leading edge of nuclei when crossing obstacles^{34,66} and a requirement for actomyosin contractility only at the front of the nucleus when crossing a transwell pore.⁷⁶ Intriguingly, we observed pulsatile fluctuations in FRET at the front of the nucleus during 3D cell migration, which may be indicative of an actomyosin-dependent tugging effect.

Actin cytoskeleton networks transmit forces over long ranges.^{77–79} Our results show that the depletion of β Pix or Myo18A leads to a complete loss of nuclear force coupling, establishing that force transmission from adhesion to nucleus in 3D matrix exists, and its loss may lead to an inability for cells to move in dense 3D matrices.

Why may β Pix/Myo18A be required for nuclear force coupling? The actomyosin networks show a polarized distribution of NM2 isoforms that are thought to have specialized functions in the migration process^{31,36}; Myo18A was shown to form heteromultimers with NM2A in cells.⁶⁸ Staining of NM2A and NM2B in invasive MDA-MB231 cells in matrix revealed a pronounced gradient, with NM2B concentrated around the nucleus and NM2A enriched more toward the protrusive region. Interestingly, NM2A was particularly enriched in the protrusive tips of pseudopodia in 3D matrices, where novel adhesion sites were forming. Disruption of the β Pix/Myo18A module resulted not only in the loss of NM2A accumulation in the vicinity of adhesions but also in a redistribution of NM2B throughout the cell. β Pix/Myo18A-dependent recruitment of NM2A to IACs may be the initial cue that instigates a self-sorting mechanism for NM2 isoforms that results in their polarized distribution previously described for cells on 2D surfaces.^{31,32,69} This self-organizing mechanism is thought to be due to the differences in NM2A/B biochemical and biophysical properties as well as expression levels. Comparatively higher NM2A expression is supposed to lead to preferential NM2A recruitment to new actin filaments at the leading edge. Because we do not observe any decrease in NM2A/B mRNA or protein levels following β Pix/Myo18A depletion, the loss of NM2A/B polarity in our system is unlikely due to differences in expression levels. In addition, we do not identify any differences in MLC phosphorylation; thus, the mislocalization of NM2A/B does not seem to be due to a defect in

Figure 6. NM2A/B polarity requires nuclear force transmission mediated through β Pix and Myo18A

(A) Representative images of MDA-MB-231 cells treated with siNT, β Pix-siRNA, or Myo18A-siRNA embedded in collagen/fibronectin gels (blue) stained for NM2B (magenta) and actin (green). Scale bars, 20 μ m.

(B) Dot plot shows average perinuclear NM2B intensity as a ratio of whole-cell NM2B intensity. One-way ANOVA; Dunnett's multiple comparison post-test versus siNT to estimate p values. *p < 0.05; ***p < 0.001. Data represent n = 38–40 cells per condition, N = 4 independent experiments.

(C) Representative images of MDA-MB-231 cells expressing GFP or GFP-DN-KASH embedded in collagen/fibronectin gels, stained for DAPI (blue) and NM2B (magenta). GFP shown in green. Scale bars, 10 μ m.

(D) Dot plot shows average perinuclear NM2B intensity as a ratio of whole-cell NM2B intensity (quantified as in Figure 5E). Two-sample t test was used to estimate p values. **p < 0.01. Data represent n = 58–60 cells per condition, N = 5 independent experiments.

(E) Model of NM2A/B gradient formation. Git1/ β Pix are recruited to nascent adhesion complexes containing paxillin at the protruding front of the cell ("relaxed nascent"). Myo18A is recruited via β Pix. Myo18A coassembles with NM2A. The tension generated by NM2A results in maturation of associated adhesion complexes, opening paxillin ("under tension"). The recruitment of NM2A to the leading edge of the invading cell promotes the formation of a front-rear NM2A/B gradient. Nesprins present on the outer nuclear membrane are able to bind to actin, and via their binding to SUN domain-containing proteins present on the inner nuclear membrane, they connect the cytoskeleton and nucleoskeleton as part of the LINC complex. An actin crosslinker is required for polarity maintenance and nuclear positioning. Mechanical integration of perinuclear actin with the nucleoskeleton is essential for the establishment of a front-rear NM2A/NM2B gradient. We propose that mechanical coupling between the nucleus and the adhesion sites is required for the establishment of this gradient and for the polarization of the invading cell. Figure created with [BioRender.com](https://www.biorender.com).

regulation, although we have not analyzed all of the potential mechanisms for NM2 activation. Instead, our data argues for a model in which β Pix/Myo18A are required for the recruitment of NM2A to adhesion sites and give rise to the formation of a NM2 isoform gradient according to previously postulated rules of self-organization and nuclear force coupling via the LINC complex.

NM2A can form heteromultimers with Myo18A in cells.⁶⁸ The anterior accumulation of NM2A in 3D embedded cells is known to stabilize protrusions,⁸⁰ and NM2A has faster motor activity than NM2B,²⁸ suggesting that NM2A is more efficient at creating contractile forces. This leads to directional force inputs into the connected actomyosin system from the leading edge of pseudopodia and the possibility of orienting polarity. By contrast, NM2B is critical for the translocation of nuclei through restrictive pores in MDA-MB-231 cells.³⁶ The requirement of NM2B around the nucleus is likely due to its higher duty ratio and the longer time NM2B spends on actin filaments, which can help generate and maintain sustained tensile force.^{28,30,81,82} Recent studies have shown that actin cross-linkers, such as α -actinin, are required for the coherence and force connectivity of the whole actin network.⁷⁸ They are also required for cell polarity and nuclear positioning.⁷⁸ This strengthens the argument for a connected actin network driving nuclear force coupling.

The directional force inputs from adhesion to the nucleus through the NM2 isoform gradient need to be proportional. How adhesion maturation is regulated to limit actomyosin force coupling through NM2A is unknown. The accumulation of β Pix in adhesions that experience a loss of tension has been reported.⁵ We wanted to find out whether the β Pix/Myo18A recruitment plays a role in adhesion maturation. β Pix is in a complex with Git1,⁵⁰ and recruitment of the β Pix-Git1 complex to adhesions is facilitated through binding of a C-terminal Git1 helix bundle to the LD2 and LD4 domains of paxillin.⁵⁵ Our experiments show that depletion of Myo18A and loss of actomyosin contractility lead to an accumulation of β Pix and Git1 in adhesions. To establish whether this accumulation is purely caused by the Git1 paxillin-binding domain, we expressed the isolated Git1-paxillin-binding domain in cells. The isolated domain mirrored the behaviors of β Pix and Git1 and accumulated in adhesions when actomyosin tension was lost. This points toward negative regulation of the paxillin binding of Git1/ β Pix after force application. The paxillin LD2 and LD4 domains are separated by 105 residues, and to simultaneously engage Git1, a loop would need to form that brings the LD2 and LD4 domains together. Tension, if exerted on such a loop, would pull it taut and inhibit the LD2-LD4 binding of Git1.^{55,83} This fits very well with the localization of β Pix toward the nascent front of adhesions and not the more force-bearing rear (Figure 2A). It has not been directly reported that paxillin stretches in response to contractility, but forces applied by the actin meshwork and through vinculin could lead to the loss of Git1/ β Pix binding from paxillin and constitute a self-limiting switch in actomyosin recruitment. Taken together, our findings present a model of how 3D adhesion sites tuned nuclear force coupling facilitates invasive cancer cell migration in complex environments.

Limitations of study

A limitation of the current comparative MS screens is that they are unable to identify which physicochemical parameter is responsible for inducing a given change between the chosen 2D and 3D microenvironmental conditions. Substrate rigidity is likely to account for a large proportion of the changes observed, but changes such as dimensionality, ligand density, and confirmation, as well as local curvature of the membrane between the 2D and 3D conditions may also play a role.⁸⁴ Future work should seek to deconvolve the contribution of each of these factors. Once technology has advanced enough to verify the mechanistic findings of this study in *in vivo* models, this should be investigated to see whether cells use the mechanisms identified here to migrate through tissues.

A better understanding of the matrix parameters that are important in regulating IAC composition and signaling would allow the field to develop *in vitro* ECM models that better resemble the microenvironment found *in vivo* while maintaining the minimal necessary level of complexity. It also remains to be seen how the relatively modest enrichment and depletion of IAC components in 2D versus 3D mass spectrometry samples will compare with future studies. At this time, we cannot predict what the maximum enrichment, based on a free pool of total expressed protein numbers, could be. A further limitation of the study is the fact that the 2D versus 3D adhesion immunofluorescence comparisons of β Pix and Myo18A were not performed with the same adhesion marker as control staining, paxillin, and VASP, respectively, due to primary antibody species overlap. This makes a comparison of the relative enrichment of β Pix and Myo18A to each other less certain.

STAR★METHODS

Detailed methods are provided in the online version of this paper and include the following:

- KEY RESOURCES TABLE
- RESOURCE AVAILABILITY
 - Lead contact
 - Materials availability
 - Data and code availability
- EXPERIMENTAL MODEL AND SUBJECT DETAILS
 - Cell culture
 - Generation of stable BiOD2 expressing cell lines:
- METHOD DETAILS
 - Isolation of 3D adhesion complexes
 - Lysate extraction
 - Pull-down of biotinylated proteins
 - Extraction of type I collagen
 - Fluorescent labelling of collagen
 - Mass spectrometry sample preparation
 - RNA-sequencing analysis
 - DNA transfections
 - 3D cell embedding
 - siRNA treatment
 - Immunofluorescence staining
 - Transwell inverted invasion assay
 - Rac/Cdc42 Pull-down assays

- Western blot analysis
- Chemical treatments
- DQ™ collagen assay
- Wound healing assay
- Circular invasion assay
- Internal polarity assay
- Centrosome polarisation assay
- Imaging details
- TIRF imaging
- FRET Imaging
- **QUANTIFICATION AND STATISTICAL ANALYSIS**
 - Mass spectrometry data analysis
 - Paxillin/Git1/βPix/Myosin18A intensity
 - Membrane proximal βPix staining
 - Invasion assay (Cell Invasion Index)
 - Circular invasion assay
 - Wound healing analysis
 - Gelatin degradation
 - Collagenase activity
 - Centrosome polarisation assay
 - Actin protrusion length
 - Nuclear circularity
 - FRET data analysis
 - Presence of NM2A in protrusions

SUPPLEMENTAL INFORMATION

Supplemental information can be found online at <https://doi.org/10.1016/j.celrep.2023.113554>.

ACKNOWLEDGMENTS

We thank the Liverpool Biomedical Imaging Facility, the Centre for Cellular Imaging (BBSRC [Biotechnology and Biological Sciences Research Council] grant BB/M012441/1), and the Centre for Genomic Research for their support and access to equipment. The mNeonGreen cDNA was used under a license agreement with Allele Biotechnology and Pharmaceuticals. L.M. thanks Cancer Research UK for core funding. P.C. was funded by the Wellcome Trust Centre for Cell-Matrix Research by grant 203128/Z/16/Z. D.N. was funded by Wellcome Trust PhD studentships (105350/Z/14/A). L.Y. was funded by MRC project grant MR/S008632/1 (to T.Z.). T.W. was funded by the Discovery Medicine North Biotechnology and Biological Sciences Research Council doctoral training program (BB/M011186/1/1797330). E.M. was funded by a North West Cancer Research grant (CR1032; to T.Z.). L.B. was funded by a Breast Cancer Now grant (2014MayPR292; to T.Z.). K.W. was funded by North West Cancer Research grants CR1010 and CR1143.

AUTHOR CONTRIBUTIONS

Conceptualization: D.N., L.Y., T.W., B.T.G., L.M., M.M., and T.Z. Methodology: D.N., L.Y., T.S., T.Y., M.M., and T.Z. Software: D.N., L.Y., and T.W. Validation: D.N., L.Y., T.W., K.W., A.C.O., E.M., L.B., and T.Z. Formal analysis: D.N., L.Y., T.W., L.B., E.M., M.M., and T.Z. Investigation: D.N., L.Y., T.W., K.W., A.C.O., E.M., P.C., L.B., T.S., T.Y., and T.Z. Resources: L.M., M.M., P.C., T.Y., and T.Z. Writing—original draft: D.N., L.Y., T.W., and T.Z. Data curation: D.N., L.Y., T.W., M.M., and T.Z. Visualization: D.N., L.Y., and T.Z. Supervision, project, and funding acquisition: L.M., T.Y., M.M., and T.Z.

DECLARATION OF INTERESTS

The authors declare no competing interests.

INCLUSION AND DIVERSITY

We support inclusive, diverse, and equitable conduct of research.

Received: June 23, 2022

Revised: June 23, 2023

Accepted: November 20, 2023

REFERENCES

1. Caswell, P.T., and Zech, T. (2018). Actin-Based Cell Protrusion in a 3D Matrix. *Trends Cell Biol.* 28, 823–834.
2. van Helvert, S., Storm, C., and Friedl, P. (2018). Mechanoreciprocity in cell migration. *Nat. Cell Biol.* 20, 8–20.
3. Jones, M.C., Humphries, J.D., Byron, A., Millon-Frémillon, A., Robertson, J., Paul, N.R., Ng, D.H.J., Askari, J.A., and Humphries, M.J. (2015). Isolation of Integrin-Based Adhesion Complexes. *Curr. Protoc. Cell Biol.* 66, 9–8.
4. Humphries, J.D., Byron, A., Bass, M.D., Craig, S.E., Pinney, J.W., Knight, D., and Humphries, M.J. (2009). Proteomic analysis of integrin-associated complexes identifies RCC2 as a dual regulator of Rac1 and Arf6. *Sci. Signal.* 2, ra51.
5. Kuo, J.-C., Han, X., Hsiao, C.-T., Yates, J.R., 3rd, and Waterman, C.M. (2011). Analysis of the myosin-II-responsive focal adhesion proteome reveals a role for β-Pix in negative regulation of focal adhesion maturation. *Nat. Cell Biol.* 13, 383–393.
6. Schiller, H.B., Friedel, C.C., Boulegue, C., and Fässler, R. (2011). Quantitative proteomics of the integrin adhesome show a myosin II-dependent recruitment of LIM domain proteins. *EMBO Rep.* 12, 259–266.
7. Chastney, M.R., Lawless, C., Humphries, J.D., Warwood, S., Jones, M.C., Knight, D., Jorgensen, C., and Humphries, M.J. (2020). Topological features of integrin adhesion complexes revealed by multiplexed proximity biotinylation. *J. Cell Biol.* 219, e202003038.
8. Rossier, O., Ochteau, V., Sibarita, J.B., Leduc, C., Tessier, B., Nair, D., Gatterdam, V., Destaing, O., Albigès-Rizo, C., Tampé, R., et al. (2012). Integrins beta1 and beta3 exhibit distinct dynamic nanoscale organizations inside focal adhesions. *Nat. Cell Biol.* 14, 1057–1067.
9. Kanchanawong, P., Shtengel, G., Pasapera, A.M., Ramko, E.B., Davidson, M.W., Hess, H.F., and Waterman, C.M. (2010). Nanoscale architecture of integrin-based cell adhesions. *Nature* 468, 580–584.
10. Humphries, J.D., Paul, N.R., Humphries, M.J., and Morgan, M.R. (2015). Emerging properties of adhesion complexes: what are they and what do they do? *Trends Cell Biol.* 25, 388–397.
11. Fraley, S.I., Feng, Y., Krishnamurthy, R., Kim, D.-H., Celedon, A., Longmore, G.D., and Wirtz, D. (2010). A distinctive role for focal adhesion proteins in three-dimensional cell motility. *Nat. Cell Biol.* 12, 598–604.
12. Harunaga, J.S., and Yamada, K.M. (2011). Cell-matrix adhesions in 3D. *Matrix Biol.* 30, 363–368.
13. Cukierman, E., Pankov, R., Stevens, D.R., and Yamada, K.M. (2001). Taking Cell-Matrix Adhesions to the Third Dimension. *Science* 294, 1708–1712.
14. Yu, X., Zech, T., McDonald, L., Gonzalez, E.G., Li, A., Macpherson, I., Schwarz, J.P., Spence, H., Futó, K., Timpson, P., et al. (2012). N-WASP coordinates the delivery and F-actin-mediated capture of MT1-MMP at invasive pseudopods. *J. Cell Biol.* 199, 527–544.
15. Goult, B.T., Yan, J., and Schwartz, M.A. (2018). Talin as a mechanosensitive signaling hub. *J. Cell Biol.* 217, 3776–3784.
16. Calderwood, D.A., Campbell, I.D., and Critchley, D.R. (2013). Talins and kindlins: partners in integrin-mediated adhesion. *Nat. Rev. Mol. Cell Biol.* 14, 503–517.
17. Bakolitsa, C., Cohen, D.M., Bankston, L.A., Bobkov, A.A., Cadwell, G.W., Jennings, L., Critchley, D.R., Craig, S.W., and Liddington, R.C. (2004).

- Structural basis for vinculin activation at sites of cell adhesion. *Nature* 430, 583–586.
18. Tadokoro, S., Shattil, S.J., Eto, K., Tai, V., Liddington, R.C., de Pereda, J.M., Ginsberg, M.H., and Calderwood, D.A. (2003). Talin binding to integrin beta tails: a final common step in integrin activation. *Science* 302, 103–106.
 19. Burridge, K., and Connell, L. (1983). A new protein of adhesion plaques and ruffling membranes. *J. Cell Biol.* 97, 359–367.
 20. Vignaud, T., Copos, C., Leterrier, C., Toro-Nahuelpan, M., Tseng, Q., Mahamid, J., Blanchoin, L., Mogilner, A., Théry, M., and Kurzawa, L. (2021). Stress fibres are embedded in a contractile cortical network. *Nat. Mater.* 20, 410–420.
 21. Tojkander, S., Gateva, G., and Lappalainen, P. (2012). Actin stress fibers – assembly, dynamics and biological roles. *J. Cell Sci.* 125, 1855–1864.
 22. Müller, P.M., Rademacher, J., Bagshaw, R.D., Wortmann, C., Barth, C., van Unen, J., Alp, K.M., Giudice, G., Eccles, R.L., Heinrich, L.E., et al. (2020). Systems analysis of RhoGEF and RhoGAP regulatory proteins reveals spatially organized RAC1 signalling from integrin adhesions. *Nat. Cell Biol.* 22, 498–511.
 23. Alieva, N.O., Efremov, A.K., Hu, S., Oh, D., Chen, Z., Natarajan, M., Ong, H.T., Jégou, A., Romet-Lemonne, G., Groves, J.T., et al. (2019). Myosin IIA and formin dependent mechanosensitivity of filopodia adhesion. *Nat. Commun.* 10, 3593.
 24. Ciobanasu, C., Faivre, B., and Le Clairche, C. (2012). Actin Dynamics Associated with Focal Adhesions. *Int. J. Cell Biol.* 2012, 941292.
 25. Livne, A., and Geiger, B. (2016). The inner workings of stress fibers – from contractile machinery to focal adhesions and back. *J. Cell Sci.* 129, 1293–1304.
 26. DeMali, K.A., Barlow, C.A., and Burridge, K. (2002). Recruitment of the Arp2/3 complex to vinculin: coupling membrane protrusion to matrix adhesion. *J. Cell Biol.* 159, 881–891.
 27. Serrels, B., Serrels, A., Brunton, V.G., Holt, M., McLean, G.W., Gray, C.H., Jones, G.E., and Frame, M.C. (2007). Focal adhesion kinase controls actin assembly via a FERM-mediated interaction with the Arp2/3 complex. *Nat. Cell Biol.* 9, 1046–1056.
 28. Barua, B., Nagy, A., Sellers, J.R., and Hitchcock-DeGregori, S.E. (2014). Regulation of nonmuscle myosin II by tropomyosin. *Biochemistry* 53, 4015–4024.
 29. Kovács, M., Wang, F., Hu, A., Zhang, Y., and Sellers, J.R. (2003). Functional divergence of human cytoplasmic myosin ii: kinetic characterization of the non-muscle iia isoform. *J. Biol. Chem.* 278, 38132–38140.
 30. Kovács, M., Thirumurugan, K., Knight, P.J., and Sellers, J.R. (2007). Load-dependent mechanism of nonmuscle myosin 2. *Proc. Natl. Acad. Sci. USA* 104, 9994–9999.
 31. Vicente-Manzanares, M., Newell-Litwa, K., Bachir, A.I., Whitmore, L.A., and Horwitz, A.R. (2011). Myosin IIA/IIB restrict adhesive and protrusive signaling to generate front-back polarity in migrating cells. *J. Cell Biol.* 193, 381–396.
 32. Shutova, M.S., Asokan, S.B., Talwar, S., Assoian, R.K., Bear, J.E., and Svithkina, T.M. (2017). Self-sorting of nonmuscle myosins IIA and IIB polarizes the cytoskeleton and modulates cell motility. *J. Cell Biol.* 216, 2877–2889.
 33. Wolf, K., Te Lindert, M., Krause, M., Alexander, S., Te Riet, J., Willis, A.L., Hoffman, R.M., Figdor, C.G., Weiss, S.J., and Friedl, P. (2013). Physical limits of cell migration: control by ECM space and nuclear deformation and tuning by proteolysis and traction force. *J. Cell Biol.* 201, 1069–1084.
 34. Davidson, P.M., and Lammerding, J. (2014). Broken nuclei–lamins, nuclear mechanics, and disease. *Trends Cell Biol.* 24, 247–256.
 35. Harada, T., Swift, J., Irianto, J., Shin, J.W., Spinler, K.R., Athirasala, A., Diegmiller, R., Dingal, P.C.D.P., Ivanovska, I.L., and Discher, D.E. (2014). Nuclear lamin stiffness is a barrier to 3D migration, but softness can limit survival. *J. Cell Biol.* 204, 669–682.
 36. Thomas, D.G., Yenepalli, A., Denais, C.M., Rape, A., Beach, J.R., Wang, Y.-L., Schiemann, W.P., Baskaran, H., Lammerding, J., and Egelhoff, T.T. (2015). Non-muscle myosin IIB is critical for nuclear translocation during 3D invasion. *J. Cell Biol.* 210, 583–594.
 37. Hieda, M. (2019). Signal Transduction across the Nuclear Envelope: Role of the LINC Complex in Bidirectional Signaling. *Cells* 8, 124.
 38. Crisp, M., Liu, Q., Roux, K., Rattner, J.B., Shanahan, C., Burke, B., Stahl, P.D., and Hodzic, D. (2006). Coupling of the nucleus and cytoplasm: role of the LINC complex. *J. Cell Biol.* 172, 41–53.
 39. Padmakumar, V.C., Libotte, T., Lu, W., Zaim, H., Abraham, S., Noegel, A.A., Gotzmann, J., Foisner, R., and Karakesisoglou, I. (2005). The inner nuclear membrane protein Sun1 mediates the anchorage of Nesprin-2 to the nuclear envelope. *J. Cell Sci.* 118, 3419–3430.
 40. Lee, J.S.H., Hale, C.M., Panorchan, P., Khatao, S.B., George, J.P., Tseng, Y., Stewart, C.L., Hodzic, D., and Wirtz, D. (2007). Nuclear lamin A/C deficiency induces defects in cell mechanics, polarization, and migration. *Biophys. J.* 93, 2542–2552.
 41. Arsenovic, P.T., Ramachandran, I., Bathula, K., Zhu, R., Narang, J.D., Noll, N.A., Lemmon, C.A., Gundersen, G.G., and Conway, D.E. (2016). Nesprin-2G, a Component of the Nuclear LINC Complex, Is Subject to Myosin-Dependent Tension. *Biophys. J.* 110, 34–43.
 42. Luxton, G.W.G., Gomes, E.R., Folker, E.S., Vintinner, E., and Gundersen, G.G. (2010). Linear arrays of nuclear envelope proteins harness retrograde actin flow for nuclear movement. *Science (New York, N.Y.)* 329, 956–959.
 43. Horn, H.F., Brownstein, Z., Lenz, D.R., Shivatzki, S., Dror, A.A., Dagan-Rosenfeld, O., Friedman, L.M., Roux, K.J., Kozlov, S., Jeang, K.-T., et al. (2013). The LINC complex is essential for hearing. *The Journal of clinical investigation* 123, 740–750.
 44. Chang, W., Antoku, S., Östlund, C., Worman, H.J., and Gundersen, G.G. (2015). Linker of nucleoskeleton and cytoskeleton (LINC) complex-mediated actin-dependent nuclear positioning orients centrosomes in migrating myoblasts. *Nucleus (Austin, Tex.)* 6, 77–88.
 45. Bouzid, T., Kim, E., Riehl, B.D., Esfahani, A.M., Rosenbohm, J., Yang, R., Duan, B., and Lim, J.Y. (2019). The LINC complex, mechanotransduction, and mesenchymal stem cell function and fate. *J. Biol. Eng.* 13, 68.
 46. Kim, D.I., Jensen, S.C., Noble, K.A., Kc, B., Roux, K.H., Motamedchaboki, K., and Roux, K.J. (2016). An improved smaller biotin ligase for BioID proximity labeling. *Mol. Biol. Cell* 27, 1188–1196.
 47. Horton, E.R., Humphries, J.D., James, J., Jones, M.C., Askari, J.A., and Humphries, M.J. (2016). The integrin adhesome network at a glance. *J. Cell Sci.* 129, 4159–4163.
 48. Brown, M.C., and Turner, C.E. (2004). Paxillin: Adapting to Change. *Physiol. Rev.* 84, 1315–1339.
 49. Klapholz, B., and Brown, N.H. (2017). Talin – the master of integrin adhesions. *J. Cell Sci.* 130, 2435–2446.
 50. Zhao, Z.S., Manser, E., Loo, T.H., and Lim, L. (2000). Coupling of PAK-interacting exchange factor PIX to GIT1 promotes focal complex disassembly. *Mol. Cell Biol.* 20, 6354–6363.
 51. Ahn, S.J., Chung, K.W., Lee, R.A., Park, I.A., Lee, S.H., Park, D.E., and Noh, D.Y. (2003). Overexpression of betaPix-a in human breast cancer tissues. *Cancer Lett.* 193, 99–107.
 52. Hsu, R.M., Hsieh, Y.J., Yang, T.H., Chiang, Y.C., Kan, C.Y., Lin, Y.T., Chen, J.T., and Yu, J.S. (2014). Binding of the extreme carboxyl-terminus of PAK-interacting exchange factor β (β PIX) to myosin 18A (MYO18A) is required for epithelial cell migration. *Biochim. Biophys. Acta* 1843, 2513–2527.
 53. Hsu, R.-M., Tsai, M.-H., Hsieh, Y.-J., Lyu, P.-C., and Yu, J.-S. (2010). Identification of MYO18A as a novel interacting partner of the PAK2/ β PIX/GIT1 complex and its potential function in modulating epithelial cell migration. *Mol. Biol. Cell* 21, 287–301.
 54. Oh, W.K., Yoo, J.C., Jo, D., Song, Y.H., Kim, M.G., and Park, D. (1997). Cloning of a SH3 Domain-Containing Proline-Rich Protein, p85SPR, and Its Localization in Focal Adhesion. *Biochem. Biophys. Res. Commun.* 235, 794–798.

55. Zhang, Z.M., Simmerman, J.A., Guibao, C.D., and Zheng, J.J. (2008). GIT1 paxillin-binding domain is a four-helix bundle, and it binds to both paxillin LD2 and LD4 motifs. *J. Biol. Chem.* **283**, 18685–18693.
56. Schmalzigaug, R., Phee, H., Davidson, C.E., Weiss, A., and Premont, R.T. (2007). Differential Expression of the ARF GAP Genes GIT1 and GIT2 in Mouse Tissues. *J. Histochem. Cytochem.* **55**, 1039–1048.
57. Manser, E., Loo, T.-H., Koh, C.-G., Zhao, Z.-S., Chen, X.-Q., Tan, L., Tan, I., Leung, T., and Lim, L. (1998). PAK Kinases Are Directly Coupled to the PIX Family of Nucleotide Exchange Factors. *Mol. Cell* **1**, 183–192.
58. Aghazadeh, B., Zhu, K., Kubiseski, T.J., Liu, G.A., Pawson, T., Zheng, Y., and Rosen, M.K. (1998). Structure and mutagenesis of the Dbl homology domain. *Nat. Struct. Biol.* **5**, 1098–1107.
59. Hodgson, L., Shen, F., and Hahn, K. (2010). Biosensors for characterizing the dynamics of rho family GTPases in living cells. *Current Protocols in Cell Biol.* Chapter 14, Unit-14.11.26.
60. Itoh, R.E., Kurokawa, K., Ohba, Y., Yoshizaki, H., Mochizuki, N., and Matsuda, M. (2002). Activation of Rac and Cdc42 Video Imaged by Fluorescent Resonance Energy Transfer-Based Single-Molecule Probes in the Membrane of Living Cells. *Mol. Cell Biol.* **22**, 6582–6591.
61. Hiroyasu, S., Stimac, G.P., Hopkinson, S.B., and Jones, J.C.R. (2017). Loss of β -PIX inhibits focal adhesion disassembly and promotes keratinocyte motility via myosin light chain activation. *J. Cell Sci.* **130**, 2329–2343.
62. Ridley, A.J., Schwartz, M.A., Burridge, K., Firtel, R.A., Ginsberg, M.H., Borisy, G., Parsons, J.T., and Horwitz, A.R. (2003). Cell Migration: Integrating Signals from Front to Back. *Science* **302**, 1704–1709.
63. Lombardi, M.L., Jaalouk, D.E., Shanahan, C.M., Burke, B., Roux, K.J., and Lammerding, J. (2011). The interaction between nesprins and sun proteins at the nuclear envelope is critical for force transmission between the nucleus and cytoskeleton. *J. Biol. Chem.* **286**, 26743–26753.
64. Infante, E., Castagnino, A., Ferrari, R., Monteiro, P., Agüera-González, S., Paul-Gilloteaux, P., Domingues, M.J., Maiuri, P., Raab, M., Shanahan, C.M., et al. (2018). LINC complex-Lis1 interplay controls MT1-MMP matrix digest-on-demand response for confined tumor cell migration. *Nat. Commun.* **9**, 2443.
65. Woroniuk, A., Porter, A., White, G., Newman, D.T., Diamantopoulou, Z., Waring, T., Rooney, C., Strathdee, D., Marston, D.J., Hahn, K.M., et al. (2018). STEF/TIAM2-mediated Rac1 activity at the nuclear envelope regulates the perinuclear actin cap. *Nat. Commun.* **9**, 2124.
66. Davidson, P.M., Battistella, A., Déjardin, T., Betz, T., Plastino, J., Borghi, N., Cadot, B., and Sykes, C. (2020). Nesprin-2 accumulates at the front of the nucleus during confined cell migration. *EMBO Rep.* **21**, e49910.
67. Janota, C.S., Calero-Cuenca, F.J., and Gomes, E.R. (2020). The role of the cell nucleus in mechanotransduction. *Curr. Opin. Cell Biol.* **63**, 204–211.
68. Billington, N., Beach, J.R., Heissler, S.M., Rimmert, K., Guzik-Lendrum, S., Nagy, A., Takagi, Y., Shao, L., Li, D., Yang, Y., et al. (2015). Myosin 18A Coassembles with Nonmuscle Myosin 2 to Form Mixed Bipolar Filaments. *Curr. Biol.* **25**, 942–948.
69. Raab, M., and Discher, D.E. (2017). Matrix rigidity regulates microtubule network polarization in migration. *Cytoskeleton* **74**, 114–124.
70. Young, L.E., and Higgs, H.N. (2018). Focal Adhesions Undergo Longitudinal Splitting into Fixed-Width Units. *Curr. Biol.* **28**, 2033–2045.e5.
71. Horton, E.R., Byron, A., Askari, J.A., Ng, D.H.J., Millon-Frémillon, A., Robertson, J., Koper, E.J., Paul, N.R., Warwood, S., Knight, D., et al. (2015). Definition of a consensus integrin adhesome and its dynamics during adhesion complex assembly and disassembly. *Nat. Cell Biol.* **17**, 1577–1587.
72. Dong, J.M., Tay, F.P.L., Swa, H.L.F., Gunaratne, J., Leung, T., Burke, B., and Manser, E. (2016). Proximity biotinylation provides insight into the molecular composition of focal adhesions at the nanometer scale. *Sci. Signal.* **9**, rs4.
73. Kutys, M.L., and Yamada, K.M. (2014). An extracellular-matrix-specific GEF-GAP interaction regulates Rho GTPase crosstalk for 3D collagen migration. *Nat. Cell Biol.* **16**, 909–917.
74. Makowska, K.A., Hughes, R.E., White, K.J., Wells, C.M., and Peckham, M. (2015). Specific Myosins Control Actin Organization, Cell Morphology, and Migration in Prostate Cancer Cells. *Cell Rep.* **13**, 2118–2125.
75. Lomakin, A.J., Cattin, C.J., Cuvelier, D., Alraies, Z., Molina, M., Nader, G.P.F., Srivastava, N., Sáez, P.J., Garcia-Arcos, J.M., Zhitnyak, I.Y., et al. (2020). The nucleus acts as a ruler tailoring cell responses to spatial constraints. *Science* **370**, eaba2894.
76. Xia, Y., Pfeifer, C.R., Zhu, K., Irianto, J., Liu, D., Pannell, K., Chen, E.J., Dooling, L.J., Tobin, M.P., Wang, M., et al. (2019). Rescue of DNA damage after constricted migration reveals a mechano-regulated threshold for cell cycle. *J. Cell Biol.* **218**, 2545–2563.
77. Hu, S., Dasbiswas, K., Guo, Z., Tee, Y.H., Thiagarajan, V., Hersen, P., Chew, T.L., Safran, S.A., Zaidel-Bar, R., and Bershadsky, A.D. (2017). Long-range self-organization of cytoskeletal myosin II filament stacks. *Nat. Cell Biol.* **19**, 133–141.
78. Senger, F., Pitaval, A., Ennomani, H., Kurzawa, L., Blanchoin, L., and Théry, M. (2019). Spatial integration of mechanical forces by α -actinin establishes actin network symmetry. *J. Cell Sci.* **132**, jcs236604.
79. Owen, L.M., Adhikari, A.S., Patel, M., Grimmer, P., Leijnse, N., Kim, M.C., Notbohm, J., Franck, C., and Dunn, A.R. (2017). A cytoskeletal clutch mediates cellular force transmission in a soft, three-dimensional extracellular matrix. *Mol. Biol. Cell* **28**, 1959–1974.
80. Rai, V., Thomas, D.G., Beach, J.R., and Egelhoff, T.T. (2017). Myosin IIA Heavy Chain Phosphorylation Mediates Adhesion Maturation and Protrusion in Three Dimensions. *J. Biol. Chem.* **292**, 3099–3111.
81. Kovács, M., Wang, F., Hu, A., Zhang, Y., and Sellers, J.R. (2003). Functional divergence of human cytoplasmic myosin II: kinetic characterization of the non-muscle IIA isoform. *J. Biol. Chem.* **278**, 38132–38140.
82. Wang, F., Kovacs, M., Hu, A., Limouze, J., Harvey, E.V., and Sellers, J.R. (2003). Kinetic mechanism of non-muscle myosin IIB: functional adaptations for tension generation and maintenance. *J. Biol. Chem.* **278**, 27439–27448.
83. Lulo, J., Yuzawa, S., and Schlessinger, J. (2009). Crystal structures of free and ligand-bound focal adhesion targeting domain of Pyk2. *Biochem. Biophys. Res. Commun.* **383**, 347–352.
84. Matellan, C., and Del Río Hernández, A.E. (2019). Engineering the cellular mechanical microenvironment – from bulk mechanics to the nanoscale. *J. Cell Sci.* **132**, jcs229013.
85. Mellacheruvu, D., Wright, Z., Couzens, A.L., Lambert, J.-P., St-Denis, N.A., Li, T., Miteva, Y.V., Hauri, S., Sardi, M.E., Low, T.Y., et al. (2013). The CRAPome: a contaminant repository for affinity purification–mass spectrometry data. *Nat Methods* **10**, 730–736.

STAR★METHODS

KEY RESOURCES TABLE

REAGENT or RESOURCE	SOURCE	IDENTIFIER
Antibodies		
Mouse monoclonal anti-paxillin	BD biosciences	Cat# 610569; RRID:AB_397918
Polyclonal rabbit Anti-βPix	Millipore	Cat# 07-1450-L
Rabbit polyclonal anti-myosin Heavy Chain 9	Cell Signaling Technology	Cat# 3403; RRID:AB_2147297
Mouse monoclonal anti-myosin Heavy chain 10 (3H2)	Abcam	Cat# ab684; RRID:AB_305661
Rabbit Polyclonal anti-pericentrin	Abcam	Cat# ab4448; RRID:AB_304461
Mouse monoclonal YAP antibody	Santa Cruz Biotechnology	Cat# sc101199; RRID:AB_1131430
Rat monoclonal anti-α5β1-integrin	Gift from Martin Humphries, University of Manchester	https://rupress.org/jcb/article-pdf/117/2/437/1470573/437.pdf
Rabbit polyclonal anti-Git1	Novus	Cat# NBP1-86144; RRID:AB_11022781
Alexa-Fluor® 594 anti-mouse	Thermo	Cat# A-11032; RRID:AB_2534091
Alexa Fluor®-680 conjugated streptavidin, 1.8 mg/mL	Jackson ImmunoResearch	Cat# 016-620-084; RRID:AB_2337252
Monoclonal mouse anti-Myosin18A,	Santa Cruz	Cat# 365328; RRID:AB_10841437
Monoclonal mouse anti-Cdc42 monoclonal antibody,	Cytoskeleton	Cat# ACD03; RRID:AB_10716593
anti-Rac1	Cytoskeleton	Cat# ARC03; RRID:AB_10709099
Polyclonal rabbit anti-GAPDH,	EMD Millipore	Cat# AB2302; RRID:AB_10615768
Monoclonal mouse anti-phospho-myosin-light-chain	Cell Signaling	Cat# 3675; RRID:AB_2250969
myosin-light-chain,	Cell Signaling	Cat# 8505S; RRID:AB_2728760
Alexa-Fluor® 488 anti-mouse	Thermo	Cat# A28175; RRID:AB_2536161
Alexa-Fluor® 670 anti-mouse	Thermo	Cat# A-21235; RRID:AB_2535804
Rabbit anti- VASP (9A2)	Cell Signaling Technology	Cat# 3132S; RRID:AB_2213393
Chemicals, peptides, and recombinant proteins		
<i>para</i> -amino-blebbistatin	Cayman Chemical	Item No. 22699
CT-1746	UCB CellTech	N/A
Y-27632	Tocris	Cat. No. 1254
ML-7	Tocris	Cat. No. 4310
Fibronectin	Sigma	FL1141
Lullaby® transfection reagent	Oz-Bioscience	LL71000
Lipofectamine ® RNAiMAX	Thermo Fisher Scientific	Catalog number: 13778075
EGF	Thermo Fisher Scientific	E4127
GM6001	Sigma	CC1000
HALT protease and phosphatase inhibitor	Thermo Fisher Scientific	Catalog number: 78440
Atto-647N-NHS-ester	Sigma-Aldrich	18373
Formaldehyde	Electron Microscopy Services	15700
Bovine serum albumin	Sigma Aldrich	A7906-10G
Acti-Stain 670 Phalloidin	Cytoskeleton	PHDN1
Hoechst	Thermo	H21486
Texas Red® conjugated Phalloidin	Thermo	T7471
Porcine trypsin	Promega	No:V5280
Acetonitrile	Sigma-Aldrich	34851
Acetone	Sigma-Aldrich	00583

(Continued on next page)

Continued

REAGENT or RESOURCE	SOURCE	IDENTIFIER
β-Mercaptoethanol	Sigma-Aldrich	M3148
Biotin	Sigma-Aldrich	B4639
DL-Dithiothreitol	Sigma-Aldrich	D5545
Diaminoethanetetra-acetic acid disodium salt dihydrate	Fisher	D/0700/53
Glycine	Fisher	G/P460/53
Iodoacetamide	Sigma-Aldrich	I1149
HEPES Buffer (1M)	Sigma-Aldrich	H0887
Lithium Chloride	Fisher (Acros Organics)	199881000
Methanol	Fisher	M/4000/PC17
Normal Donkey Serum	Sigma-Aldrich	D9663
NP-40 - Nonidet™ P 40 Substitute	Sigma-Aldrich	74385
Sodium deoxycholate	Sigma-Aldrich	30970
Sodium dodecyl sulfate	Fisher	S/5200/53
Tris-base	Fisher	BP152-1
Triton X-100	Sigma-Aldrich	X100
Trizma® hydrochloride	Sigma-Aldrich	T3253
Tween 20	Fisher	BP337-500
Pierce™ NeutrAvidin™ agarose beads	Thermo Scientific	29200
Dimethyl Sulfoxide	Sigma-Aldrich	D2650
Critical commercial assays		
DQ™ collagen	Invitrogen	D12060
SiR-tubulin	Spirochrome	cat#: SC002
Cdc42 Activation Assay Biochem Kits	Cytoskeleton, Inc.	SKU: BK034-S
Rac1 Activation Assay Biochem Kits	Cytoskeleton, Inc.	SKU: BK035-S
Clarity Western ECL Substrate	Biorad	1705061
SiR-Actin	Spirochrome	cat#: SC001
Pierce™ NeutrAvidin™ agarose beads	Thermo	Catalog number: 29200
BCA Protein assay	Thermo	23225
NEBNext® Ultra™ Directional RNA Library Prep Kit for Illumina	New England Biolab	Discontinued
LookOut Mycoplasma PCR detection kit	Sigma	MP0035
Nucleofector™ II system Kit V	Lonza	VCA-1003
TransIT®-2020	Mirus	MIR 5400
InstantBlue® Coomassie Protein Stain	Abcam	ab119211
miRNeasy kit	Qiagen	ID: 217084
Deposited data		
mass spectrometry data	This study	[PRIDE]:[PXD043063]
Experimental models: Cell lines		
Human MDA-MB-231 (HTB-26™)	ATCC	https://www.atcc.org/products/htb-26
Human osteosarcoma U2OS cells (HTB-96™)	ATCC	https://www.atcc.org/products/htb-96
MDA-MB-231-mNeonNM2A	This study	N/A
Oligonucleotides		
	Table S1 for oligos	N/A
Recombinant DNA		
pcDNA3.1 mycBioID	Addgene	# 35700
myc-BioID2-MCS	Addgene	plasmid # 74223
MCS-13X-Linker-BioID2-HA	Addgene	80899

(Continued on next page)

Continued

REAGENT or RESOURCE	SOURCE	IDENTIFIER
mApple-Paxillin-22	Addgene	#54935
mini nesprin2 tension sensor	Woroniuk et al. 2018 ⁶⁵	N/A
Raichu-Rac1	gift from Patrick Caswell, Itoh et al., 2002 ⁶⁰	N/A
Raichi-Cdc42	gift from Patrick Caswell, original Itoh et al., 2002 ⁶⁰	N/A
GFP-Myosin18Aalpha	Gift from Martin Humphries, University of Manchester	N/A
mCherry-Talin-1	Gift from David Critchley, University of Leicester	N/A
GFP-Paxillin	Gift from Patrick Caswell, University of Manchester	N/A
mCherry-Vinculin	Gift from Christoph Ballestrem, University of Manchester	N/A
dominant-negative (tm) Nesprin	Lombardi et al. 2011, ⁶³ Gift from Akis Karakesioglou, University of Manchester	N/A
GFP-βPIX	This study	N/A
GFP-βPIX ΔM18A	Hsu et al., 2014 ⁵²	N/A
CRISPR plasmids including all-in-one CRISPR-Cas9 vector, MS2-CtIP and donor vector, PITCh-mNeonGreen-guideMYH9	This study	N/A
GFP-Git GPBR	This study	N/A
myc-BioID2-Paxillin	This study	N/A
Talin-13X-Linker-BioID2-HA	This study	N/A
PITCh-mNeonGreen-guideMYH9	This study	N/A

Software and algorithms

ImageJ/Fiji software	ImageJ	https://imagej.net/software/fiji/
SlideBook 6 software	Intelligent Imaging Innovations, Inc	https://www.intelligent-imaging.com/slidebook
CASAVA version 1.8.2	Illumina	N/A
Mascot Sever v.2.3.2	Matrix Science	N/A
Scaffold (Version 4)	Proteome Software	N/A
Cytoscape	Cytoscape Consortium	https://cytoscape.org/
CRAPome	Mellacheruvu et al. 2013, ⁸⁵ The crapome: a contaminant repository for affinity purification-mass spectrometry data. Nature Methods, 10:730	N/A
STRING V10.5	STRING Consortium	https://string-db.org/

RESOURCE AVAILABILITY

Lead contact

Further information and requests for resources and reagents should be directed to and will be fulfilled by the Lead Contact, Tobias Zech (tzech@liverpool.ac.uk).

Materials availability

Plasmids generated in this study have been deposited to Addgene.

Data and code availability

- Mass spectrometry data have been deposited at PRIDE and are publicly available as of the date of publication. Accession numbers are listed in the [key resources table](#). Original western blot images and microscopy data reported in this paper will be shared by the [lead contact](#) upon request.

- Any additional information required to reanalyze the data reported in this paper is available from the [lead contact](#) upon request.
- This paper does not report original code.

EXPERIMENTAL MODEL AND SUBJECT DETAILS

Cell culture

Human MDA-MB-231 and Human osteosarcoma U2OS cells (HTB-96TM) were obtained from ATCC®. MDA-MB-231 cells were maintained in high glucose, GlutaMAXTM, DMEM (Gibco, Thermo Scientific, 31966047) supplemented with 10% Fetal bovine serum (Sigma-Aldrich) at 37°C and 5% CO₂. Cell lines were tested at regular intervals for mycoplasma contamination using LookOut Mycoplasma PCR detection kit (Sigma-Aldrich). All cell lines were used for a maximum of 25 passages.

Generation of stable BioID2 expressing cell lines:

MDA-MB-231 cells were transfected with BioID2 using a Nucleofector II system (Lonza) according to manufacturer's instructions (Program X-013, Kit V). After 2 days cells were selected with G418 (2 mg/mL, Sigma-Aldrich). Once visible colonies had formed (~3–4 weeks) individual colonies were picked and sub-cultured. Individual colonies were then tested for expression of BioID2-construct expression via Western blotting.

CRISPR knock-in cell line generation: The CRISPR-knock-in MDA-MB-231 cell line expressing mNeon-NM2A (named "231-mNeonNM2A") was made by CRISPR-Cas9. CRISPR plasmids were transfected into MDA-MB-231 cells using TransIT-2020 (Mirus Bio) transfection reagent in equal amounts. Clones were selected by FACS sorting and single cell cloning, then verified by immunofluorescence and western blotting.

METHOD DETAILS

Isolation of 3D adhesion complexes

Labeling of adhesions complexes: MDA-MB-231 cells expressing BioID2 constructs were either seeded on to Fibronectin/Collagen coated 10 cm (plastic tissue culture dishes) or embedded in 1.7 mg/mL collagen hydrogel supplemented with fibronectin. Cells were allowed to spread for 4 h before the culture medium was supplemented with 50 μM biotin. Cells were then incubated with biotin for 16 h prior to lysate extraction.

Lysate extraction

2D and 3D samples were washed twice in 4°C PBS(–), followed by 4°C 50 mM EDTA PBS(–). 2D and 3D samples were then rocked at 4°C for 1 h. Collagen gels were centrifuged for 1 min at 3200 x g at 4°C and the supernatant removed. RIPA lysis buffer (150 mM NaCl, 1% (v/v) NP-40, 0.5% (w/v) Sodium deoxycholate, 0.1% Sodium dodecyl sulfate, 50 mM Tris pH 8.0, supplemented with 1x HALT protease and phosphatase inhibitor (Thermo Fisher Scientific)) was then added to each sample. Samples for each condition were pooled before being repeatedly passed through a 20 mL syringe, a 1 mL syringe and a 25-gauge needle to ensure homogenisation. Samples were transferred to pre-cooled Eppendorfs and centrifuged at 14,000 x g for 15 min at 4°C. The supernatant was retained as the sample.

Pull-down of biotinylated proteins

An equal amount of protein was used for each pull-down in every condition (diluted to an equal volume in RIPA lysis buffer). 50 mM Tris pH 7.4 was added to each sample, equal to 50% of the total volume. Pierce NeutrAvidin agarose beads (Thermo Fisher Scientific) were pre-equilibrated with 2:1 RIPA lysis buffer:50 mM Tris pH 7.4. Samples and beads were rotated at 4°C overnight. To remove each wash, samples were centrifuged at 20 x g at room temperature (RT) for 1 min before removal of the supernatant. Each sample was washed with BioID Wash Buffer #1 (2% SDS in dH₂O) for 8 min on a rotator. Beads for each condition were then pooled in BioID Wash Buffer #1 and washed for 8 min. Beads were washed with 1x BioID Wash Buffer #2 (0.1% (w/v) Sodium Deoxycholate, 1% (w/v) Triton X-100, 1 mM EDTA, 500 mM NaCl, 50 mM HEPES) and 1x BioID Wash Buffer #3 (0.5% (w/v) Sodium Deoxycholate, 0.5% (w/v) NP-40, 1 mM EDTA, 250 mM LiCl, 10 mM Tris pH 7.4.) for 8 min each. Beads were then washed with 50 mM Tris pH 7.4. Proteins were eluted from the beads by the addition of a volume equal to that of the beads of 2 x reducing elution buffer. Samples were boiled for 10 min at 96°C before collection of the eluate. This was repeated a further two times. Samples were diluted 4-fold in –20°C acetone and incubated overnight at –20°C. Samples were subjected to centrifugation at 14,000 x g for 10 min at 4°C. The supernatant was removed and protein pellets were allowed to air dry in a flow hood. Samples were re-suspended in 2x reducing sample buffer.

Extraction of type I collagen

Approximately 12–14 frozen rat tails were thawed in 70% ethanol. The skin was removed and individual tendons were extracted, care was taken to avoid extracting the sheath. Tendons were dissolved in 0.5 M acetic acid at 4°C for 48 h. The tendon extract was centrifuged at 7500 x g for 30 min to remove debris. 10% (w/v) NaCl was added to the supernatant which was stirred for 1 h at 4°C. The extract was then centrifuged at 10,000 x g for 30 min. The pellet was dissolved in 0.25 M acetic acid and stirring for

24 h at 4°C. The collagen solution was dialyzed (VISKING, SERA44120, MWCO 12–14 kDa, regenerated cellulose) against 8 changes (twice daily) of 17.5 mM acetic acid. The dialyzed collagen solution was then centrifuged at 30,000 × g for 1.5 h. The collagen solution was then stored at 4°C in a sterile container for a minimum of two weeks before use in assays. Protein concentration of the collagen was verified by both BCA Protein assay (Sigma-Aldrich, cat: BCA1) and drying via vacuum centrifugation.

Fluorescent labelling of collagen

Rat tail type I collagen was diluted in 4°C PBS(+). Collagen was neutralized using 0.46 M sodium bicarbonate and a final collagen hydrogel concentration of 3 mg/mL was created. The gel was added to a 10 cm tissue culture dish and allowed to polymerise at RT for 1 h. The collagen gel was incubated with 50 mM Borate buffer (pH 9.0) for 10 min 2 mg/mL of Atto-647N-NHS-ester (Sigma-Aldrich Aldrich, cat: 18373) was diluted in 50 mM Borate buffer (pH 9.0) and added to the collagen gel for 1 h at RT, protected from light. Labeling solution was removed from the gel, and residual ester quenched by the addition of 50 mM Tris pH 7.4 for 10 min. The gel was washed 8 × 10 min with PBS(+). Labeled collagen was dissolved by incubation in 0.2 M HCl at 4°C for 4 days. Dissolved collagen was dialyzed against 20 mM acetic acid overnight. When used in assays a small amount of labeled collagen (between 0.5% and 2% of total volume) was added into the prepared collagen solution, as indicated.

Mass spectrometry sample preparation

Samples were separated by polyacrylamide gel electrophoresis. Polyacrylamide gels were stained with Instant Blue protein dye (Abcam) for 45 min, and then washed with ddH₂O. Each sample was cut into 15 slices by hand using a clean glass tile and sterile scalpel. Slices were cut into cubes approximately 1 mm³ in size and transferred into a perforated 96-well plate (Glygen Corp). Gel pieces were de-stained with repeated 30 min incubations of 50% (v/v) Acetonitrile (ACN)/50% 25 mM NH₄HCO₃ (v/v) at RT. Gel pieces were dehydrated by 2 × 5 min incubations with ACN followed by vacuum centrifugation. Peptides were then reduced via incubation with 10 mM dithiothreitol (DTT) at 56°C for 1 h. Peptides were then alkylated by incubation with 55 mM iodoacetamide (IA) for 45 min at RT whilst being protected from light. DTT and IA were removed by two rounds of washing and dehydration: 5 min incubations with 25 mM NH₄HCO₃ followed by a 5 min incubation with ACN. ACN was removed by centrifugation, the gel pieces were then dried via vacuum centrifugation. 1.25 ng/L Porcine trypsin (Promega, Cat No:V5280) in 25 mM NH₄HCO₃ was added to the gel pieces, which were incubated at 4°C for 45 min to allow the trypsin to permeate the gel pieces. Samples were then transferred to 37°C to allow digestion overnight. Trypsinised peptides were collected from gel pieces via centrifugation. Residual peptides were extracted with a 30 min incubation at RT with 99.8% (v/v) ACN/0.2% (v/v) formic acid and then 50% (v/v) ACN/0.1% formic acid (v/v) which were each subsequently extracted via centrifugation. The collected eluate was dried by vacuum centrifugation. Dried peptides were then stored at –20°C until resuspension prior to analysis. Dried peptides were re-suspended in 5% (v/v) ACN in 0.1% formic acid. Each sample was separated on a Nanoacquity (Waters) Ultra Performance Liquid Chromatography column coupled to an LTQ-Orbitrap XL (Thermo Fisher) equipped with a nanoelectrospray source (Proxeon). MS spectra were acquired at a resolution of 30,000 and MS/MS was performed on the top 12 most intense ions.

RNA-sequencing analysis

MDA-MB-231 cells were embedded into 1.7 mg/mL collagen supplemented with 50 μg/mL fibronectin, and total miRNA extracted using a miRNeasy kit (QIAGEN) according to the manufacturer's protocol. RNA samples were processed and sequenced by the Center for Genomic Research (University of Liverpool). 1mg of total RNA was treated for polyA using Next Ultra Directional RNA library prep kit (New England Biosciences). Enriched RNA was amplified using the ScriptSeq v2 RNA-Seq Library Preparation protocol. After 12 cycles of amplification DNA was purified using Ampure XP beads. Denatured template DNA at a concentration of 300 p.m. was sequenced using two lanes of an Illumina HiSeq2500 at 2x150 bp paired-end sequencing with v1 chemistry. Basecalling and de-multiplexing of indexed reads was performed by CASAVA version 1.8.2 (Illumina). Sequences were trimmed to remove Illumina adapter sequences using Cutadapt version 1.2.1, any reads which matched the adapter sequence over at least 3 bp were trimmed. Low quality bases were removed using Sickle version 1.200 with a minimum window quality score of 20. Finally, after trimming, all reads shorter than 10 bp were removed.

Quantification of expression of transcripts from the trimmed datasets was performed using Salmon v0.12.0 (Patro et al., 2017), transcripts were mapped against Homo Sapiens transcriptome (Version 86, EMBL). Gene level count matrices were generated and differentially expressed genes were determined using the DESeq2 package (Love et al., 2014; Sonesson et al., 2015).

DNA transfections

Cells to be transfected were seeded at 2 × 10⁵ cells per well in a 6-well plate ~16–20 h prior to transfection. MDA-MB-231 cell transfections were performed using TransIT-2020 transfection reagent or Lullaby transfection reagent (OZ Bioscience); 1 μg of each plasmid was used for all transfections (2 μg total). Cells were transfected for 24 h before imaging. Before imaging, for 2D cell culture, cells were plated onto glass bottom 35 mm dishes (SPL Confocal 35-mm clear coverglass-bottom Petri dish, #101350) pre-coated for 1 h (4°C) with 50 μg/mL collagen (as prepared below) and 10 μg/mL Fibronectin (Sigma-Aldrich, FL1141). For 3D cell culture, cells were embedded in matrices 8–18 h before imaging.

Plasmids used in this study include: pcDNA3.1 mycBioID (a gift from Kyle Roux (Addgene plasmid # 35700; <http://n2t.net/addgene:35700>; RRID:Addgene_35700), myc-BioID2-MCS (a gift from Kyle Roux (Addgene plasmid # 74223; <http://n2t.net/addgene:74223>; RRID:Addgene_74223), MCS-13X-Linker-BioID2-HA (a gift from Kyle Roux (Addgene plasmid # 80899; <http://n2t.net/addgene:80899>; RRID:Addgene_80899), mApple-Paxillin-22 (Addgene, #54935), mN2-TS (Woroniuk et al. 2018⁶⁵) Raichu-Rac1 (gift from Patrick Caswell (Itoh et al., 2002),⁶⁰ Raichi-Cdc42 (gift from Patrick Caswell, (Itoh et al., 2002),⁶⁰ GFP-Myosin18Aa (Gift from Martin Humphries, University of Manchester), mCherry-Talin-1 (Gift from David Critchley, University of Leicester), GFP-Paxillin (Gift from Patrick Caswell, University of Manchester), mCherry-Vinculin (Gift from Christoph Ballestrem, University of Manchester), dominant-negative (tm) Nesprin (Lombardi et al. 2011;⁶³ Gift from Akis Karakesioglou, University of Manchester), GFP-βPIX, GFP-βPIX Δ M18A (Zech Lab, this study; Hsu et al., 2014).⁵² CRISPR plasmids including all-in-one CRISPR-Cas9 vector, MS2-CtIP and donor vector, PITCh-mNeonGreen-guideMYH9 were designed according to (Sakuma et al., 2016).

Plasmids designed in this study: GFP-Git GPBR – N-terminal located GFP was linked to GGS and Git1 amino acids 637–761 (paxillin binding region) (designed on VectorBuilder).

Plasmids generated in this study: myc-BioID2-Paxillin was generated by the amplification of Paxillin via PCR from GFP-Paxillin using the primers TCA TGC GAA TTC ATG GAC CTC GAC GCC and TGA GAC AAG CTT CTA GCA GAA GAG CTT GAG. The PCR product and myc-BioID2-MCS were digested with EcoR1 and HindIII, purified and ligated. A start codon and Kozak sequence were introduced into MCS-13X-Linker-BioID2-HA via mutagenesis (Forward: CCC GCC TCC ACC GGA TCC CAT GGT GGA AAC ACC ATG GGA TCC GAA TTC GAA TC, Reverse: GAT TCG AAT TCG GAT CCC ATG GTG TTT CCA CCA TGG GAT CCG GTG GAG GGC GG) to produce the ATG-13X-Linker-BioID2-HA vector. To generate the Talin-13X-Linker-BioID2-HA, Talin was amplified from mCherry-Talin-1 (Forward: GAT CCA GAA TTC CAC CAT GGT TGC GCT TTC GCT G, Reverse: TGG ATC GAA TTC GTG CTC GTC TCG AAG CTC). The PCR product and MCS-13X-Linker-BioID2-HA were digested with EcoRI, purified and ligated. The all-in-one CRISPR-Cas9 vector was generated to express Cas9 and MS2-containing sgRNAs for donor cleavage and genome targeting in accordance with the previous report (Nakade et al., 2018). The inserted oligonucleotides for genome targeting were as follows: sense, CAC CGT GCA GGA GAA GAG GCT TAT T and antisense, AAA CAA TAA GCC TCT TCT CCT GCA C. The PITCh-mNeonGreen-guideMYH9 was generated by PCR and In-Fusion cloning method (Takara) to insert mNeonGreen at the 3' end of MYH9 coding sequence with 40-bp microhomologies in accordance with the previous reports (Sakuma et al., 2016; Nakade et al., 2018).

3D cell embedding

For 3D cell embedding, gels were prepared fresh on the day of use. All solutions and collagen were kept at 4°C during preparation of the gel. The required amount of rat tail type I collagen was diluted with sterile ddH₂O in order to achieve the desired final gel concentration. 10x DMEM equal to 10% of the final volume was added to the collagen gel. The pH of the gel was neutralised via the addition of 0.46 M Sodium Bicarbonate equal to 10% of the final volume. Gels were supplemented with Fibronectin (Sigma-Aldrich) to a final concentration of 10 μg/mL. The desired number of cells were trypsinised and pelleted via centrifugation. Cells were suspended in collagen/fibronectin gel solution by gentle pipetting. Cell suspensions were quickly transferred either to a cell imaging dish (SPL 35-mm dishes) or 6 well plate depending on the assay. Collagen gels were then transferred to a humidified CO₂ incubator at 37°C to allow gel polymerisation. After 1 h, full growth medium was added carefully to the top of the gels and cells were returned to 5% CO₂/37°C until imaging/fixation.

siRNA treatment

MDA-MB-231 cells: 10 nM of each siRNA oligonucleotide was introduced using Lullaby® transfection reagent (Oz Biosciences) following manufacturer's instructions. U2OS cells: 50 nM of each siRNA oligonucleotide was introduced using Lipofectamine® RNAiMAX (Thermo Fisher Scientific) following manufacturer's instructions. Oligonucleotides for siRNA included: human βPix (synthesized by Qiagen), human myosin-18A (synthesized by Qiagen):–

βPix siRNA – #1 - AACATCAACTGGTAGTAAGA (Qiagen S104239011), #2 CAAGCGCAAACCTGAACGGAA (Qiagen S104308997)

Myosin-18A siRNA – #1 CACGAAGTGGAGATGGATCTA (Qiagen SI04273668), #2 CAGTCGTGTCAGAAGAAGTTA (Qiagen S104318034)

For all knockdown experiments, cells were subjected to siRNA treatment at 24, 72 h post-seeding. Where one siRNA treatment is indicated this is a pooled siRNA mix of the siRNAs listed above. Cells were analyzed 96–120 h post-original transfection. All knockdown experiments were undertaken at least three independent times unless otherwise stated.

Immunofluorescence staining

For cells plated on 2D surfaces, at appropriate time points following cell plating, cells were fixed by removal of medium and addition of 4% PFA (Electron Microscopy Sciences, Hatfield, PA) in PBS for 20 min at RT, washed 3x with PBS, permeabilized with 0.25% Triton X-100 in PBS for 15 min, washed 3x with PBS, and incubated in blocking buffer (10% bovine serum albumin (BS)) Sigma-Aldrich, A7906 in PBS) for 30 min. For cells embedded in 3D surfaces, cells were fixed by removal of medium and addition of 4% PFA; in 0.05 M phosphate buffer, pH 7–7.2 for 40 min at RT, washed 3x with PBS, permeabilized with 0.1% Triton X-100 in PBS for 30 min, washed 3x PBS rapid wash followed by 2 × 5min PBS wash and incubated in blocking buffer for 1 h. All cells were

incubated with primary antibody (in PBS plus 10% blocking buffer) overnight at 4°C, followed by 3x PBS rapid followed by 2 × 5min PBS wash and incubation in 1/250 dilution secondary antibody +/- Acti-Stain 670 Phalloidin (Cytoskeleton, Inc.), plus Hoechst (Thermo Scientific, H3570) in PBS plus 10% blocking buffer for 4h at RT. Cells were washed in 3 x PBS rapid wash followed by 6 × 5min, and imaged immediately by confocal microscopy.

Primary antibodies: Mouse monoclonal anti-Paxillin (1:50, BD biosciences #610569), Polyclonal rabbit Anti-βPix (Millipore 1:200, 07-1450-L), Monoclonal mouse anti-Myosin18A, (1:200 SCBT 365328), Rabbit anti- VASP (9A2) (1:200 Cell Signaling Technology 3132S), Rabbit polyclonal anti-myosin Heavy Chain 9 (1:100 Cell Signaling Solution Technology #3403), Mouse monoclonal anti-myosin Heavy chain 10 (3H2) (1:200 Abcam ab684), Rabbit Polyclonal anti-pericentrin (1:2000, Abcam ab4448), Mouse monoclonal YAP antibody (1:1000, Santa Cruz Biotechnology sc-101199), Rat monoclonal anti-α5β1-integrin (1:200, Mab11, in-house purification from hybridoma), Rabbit polyclonal anti-Git1 (1:200, Novus, NBP1-86144).

Secondary antibodies: Alexa-Fluor 488, 594 & 647 anti-mouse, rabbit & rat IgG antibodies (Jackson ImmunoResearch). All secondary antibody stock solutions were diluted to a concentration of 1.7 mg/mL and used at a dilution of 1:500 (2D staining) and 1/250 (3D staining). Alexa-Fluor-647 or Texas Red conjugated Phalloidin (Molecular Probes, Invitrogen) was diluted to approximately 6.6 μM in methanol and used at a dilution of 1:400.

Transwell inverted invasion assay

Matrigel (Corning) was diluted to 5 mg/mL with PBS (-) and supplemented with fibronectin to a final concentration of 10 μg/mL. The Matrigel mixtures were polymerised in transwell inserts (Corning) at 37°C for 1 h. Inserts were then inverted and 8×10^4 cells were seeded onto the transwell filter. Cells were allowed to adhere 3–6 h before inversion of the insert. Serum-free culture medium was added to the wells of the transwell plates while culture medium containing 10% FBS and 20 ng/mL EGF (Sigma) was added to the top of the matrigel. After 5 days of culture, samples were fixed with 4% PFA for 30 min and then permeabilized by treatment with 0.1% Triton X-100 in PBS(-) for an additional 30 min. Samples were stained with DAPI and stacks imaged every 10 μm. For negative invasion controls, GM6001 (Sigma) treatment was used at 5 μM. GM6001 was added for the duration of the experiment.

Rac/Cdc42 Pull-down assays

Cdc42 and Rac1 Pull-Down assays were carried out using Cdc42/Rac1 Activation Assay Biochem Kits (Cytoskeleton, Inc.), following manufacturer's instructions. Briefly, cells were washed in ice-cold PBS and lysed in ice-cold lysis buffer supplemented with protease inhibitor cocktail following 96 h of siRNA treatment. Approximately 800 μg protein were loaded onto PAK-PBD beads and subjected to pull-down assay protocol. Samples were analyzed by SDS-page and Western blot analysis.

Western blot analysis

For detection of siRNA depletion: Cells were extracted 96–120 h post-transfection. Cells were washed 2× in ice-cold PBS and lysed in radioimmunoprecipitation assay (RIPA) buffer: 10 mM Tris-HCl, 150 mM NaCl, 1% Triton X-100 (w/v), 0.1% SDS (wt/v), and 1% sodium deoxycholate (w/v) supplemented with Halt protease and phosphatase inhibitors (Thermo Fisher Scientific) by rocking at 4°C for 10 min. Just before SDS-PAGE, the protein sample was mixed 1:5 with 5x Sample Buffer (15% SDS, 312.5 mM Tris pH 6.8, 50% Glycerol, 16% β-Mercaptoethanol). Proteins were separated by 12–20% SDS-PAGE and transferred to a polyvinylidene fluoride membrane (Millipore, Billerica, MA). The membrane was blocked with TBS-T (20 mM Tris-HCl, pH 7.6, 136 mM NaCl, and 0.1% Tween 20) containing 3% BSA for 1 h, then incubated with primary antibody at 4°C overnight. After washing with TBS-T, the membrane was incubated with HRP-conjugated secondary antibody (Bio-Rad, Hercules, CA) for 2 h at RT. Protein signal was measured by fluorescence-based detection or chemiluminescence. For fluorescence-based detection, membranes were imaged using a LICOR ODYSSEY Sa infrared imaging system. For chemiluminescence based detection, membranes were developed using Clarity Western ECL Substrate (BioRad, 1705061) according to manufacturer's instructions and imaged using a ChemiDoc Touch (BioRad) imaging system.

Primary antibodies: Polyclonal rabbit anti-βPix (Millipore 1:1000, 07-1450-L), Monoclonal mouse anti-Myosin18A (1:200, Santa Cruz, H-10, 365328), Monoclonal mouse anti-Cdc42 monoclonal antibody (1:250, Cytoskeleton, Cat. # [ACD03](#)), anti-Rac1 (1:250, Cytoskeleton, Cat. # [ACC03](#)), Rabbit polyclonal anti-Git1 (1:1000, Novus, NBP1-86144), Polyclonal rabbit anti-GAPDH (1:10,000: AB2302; EMD Millipore), Monoclonal mouse anti-phospho-myosin-light-chain (1:500, Cell Signaling #3675), myosin-light-chain (1/500, Cell Signaling #8505S). For the detection of biotin, membranes were incubated with Alexa Fluor-680 conjugated streptavidin (1.8 mg/mL, Jackson ImmunoResearch) diluted 1:2000 in 5% BSA (in TBST).

Membrane blots were incubated with either Alexa Fluor 680 or 790 conjugated (Molecular Probes, Invitrogen) or HRP conjugated (Pierce) secondary antibodies diluted 1:10000 in blocking buffer.

Chemical treatments

MDA-MB-231 or U2OS cells were pre-treated with 20 μM *para*-amino-blebbistatin (Cayman Chemical, Item No. 22699) for 1 h before imaging or fixation. Blebbistatin remained in media during live-cell imaging (with GFP-GPBR constructs). Imaging took no longer than 15 min to limit cell exposure to blebbistatin.

MDA-MB-231 were treated with 20 μ M CT1746 (UCB, CellTech) a broad-spectrum MMP inhibitor. Cells were embedded in collagen gels and treated with standard culture medium supplemented with 20 μ M CT1746 (or equivalent total volume of vehicle control) 2 h prior to fixation.

MDA-MB-231 were treated with Y-27632/ML-7 combination. Cells were embedded in collagen gels and were treated with standard culture medium supplemented with 20 μ M Y-27632 and 20 μ M ML-7 (Tocris) (or equivalent total volume of vehicle control) 2 h prior to imaging.

DQ™ collagen assay

100,000 MDA-MB-231 cells treated with the indicated siRNA were plated per well of a 24-well plate. Cells were trypsinised and re-suspended in DQ collagen (Invitrogen) to manufacturer instructions (1/1000 dilution), with collagen/fibronectin gel mix (as described in [3D cell embedding](#)). Cells were left to incubate overnight before fixation. Collagen/FITC intensity was measured as a readout of collagenase activity. For negative invasion controls, CT1746 (general MMP inhibitor) treatment was used at 20 μ M 2h prior to fixation.

Wound healing assay

U2OS cells were treated with siRNA as indicated. Cells were then cultured in monolayers in 12-well plates (3 \times 10⁵ cells per well) with culture-insert 2 well in μ -Dish 35 mm (ibidi) for 24 h before the insert was removed. Phase-contrast images were acquired with a Zeiss Widefield system equipped with 20xNA lens. Images were acquired every 30 min for a 40 h period. Wound area was determined using ImageJ software.

Circular invasion assay

MDA-MB-231 cells were treated with siRNA as indicated. Cells were then cultured in monolayers in Culture-Insert 2 Well in μ -Dish 35 mm (ibidi) before the insert was removed and 500 μ L of collagen/fibronectin gel mix was added to cover cells. Cells were left for 4 h before invasion was monitored. Cells were imaged every 1 h for a period of 24-72h.

Internal polarity assay

Coverslips with micropatterned crossbow shapes coated with fluorescent fibronectin (excitation at 650 nm) were obtained from CYTOO SA (USA). CYTOOchips were placed in a 6-well tissue culture plate and treated with culture medium before addition of cells. MDA-MB-231 cells treated with siRNA as stated, were trypsinized and diluted to a concentration of 15,000 cells per mL. 1mL cells were added to each well, and left undisturbed for 15 min, before being moved to the culture incubator for 1 h. Unattached cells were removed by multiple rounds of careful PBS(–) washing. Cells were then returned to a tissue culture incubator allowed to spread 6 h prior to fixation.

Centrosome polarisation assay

To examine centrosome polarity in gels, MDA-MB-231 cells treated with siRNA as stated were trypsinized and diluted to a concentration of 100,000 cells per ml and mixed with collagen/fibronectin gel. Cells were left for 8 h before addition of 100nM SiR-tubulin and 10 μ M Verapamil (Cytoskeleton, Inc, cat#: SC002) to standard culture medium. Cells were imaged overnight in SiR-tubulin/Verapamil containing media. Cells were left for 4 h before invasion was monitored. Cells were imaged every 15min for a period of 24-72h.

Imaging details

Unless otherwise stated, images were recorded with a Marianas spinning disk confocal microscope (3i) using a 63x 1.4 NA or 10x 0.45 NA Zeiss Plan Aplanachromat lens and either an Evolve electron-multiplying charge-coupled device (Photometrics) or FLASH4 sCMOS (Hamamatsu) camera.

TIRF imaging

Imaging of cells was carried out on the Marianas spinning disk confocal microscope with an attached motorised TIRF module (Zeiss) and α Plan-Aplanachromat 100x/1.46 oil (Zeiss) TIRF objective was used. Images were acquired using a Hamamatsu ORCA Flash 4.0 CMOS camera with 2x binning. For imaging of fixed samples via TIRF microscopy cells were seeded onto glass-bottomed cell imaging dishes (SPL 35-mm dishes). Samples were then prepared according to the protocol described above for immunofluorescence staining. With the exception that dishes were left in a final PBS wash (rather than mounting medium) and imaged immediately.

FRET Imaging

Imaging of cells for determination of FRET was carried out on the Marianas spinning disk confocal microscope, for each image, five channels were captured; one channel detecting a 447–517 nm range under a 445 nm excitement with a 1000 ms exposure (denoted 'Donor' channel), another detecting a 515–569 nm range under 514 nm excitement with a 200 ms exposure (denoted 'Acceptor' channel), a third detecting a 515–569 nm range under 445 nm excitement with a 1000 ms exposure (denoted 'Transfer' channel), and a further two channels consisting of a brightfield illumination of 100 ms and a far-red channel (652–732 nm range under 647 nm excitement with an exposure of 1000 ms) for imaging fluorescent collagen. For singular images, the laser power was set to 100%; for time-lapse images, the power was set to 20%. Images were taken once every min for time-lapse images.

QUANTIFICATION AND STATISTICAL ANALYSIS

Mass spectrometry data analysis

Obtained spectra were searched against a database containing both manually reviewed (UniProt) and unreviewed (TrEMBL) proteins (UniProt-Consortium, 2019) using Mascot Sever (version 2.3.2, Matrix Science) (Perkins et al., 1999). Mascot search results were imported into Scaffold (Version 4) for statistical analysis. Results were also searched against X!Tandem to increase confidence of protein identification. Protein and peptide confidence thresholds were set at 99% and 95%, respectively. Proteins were considered to be enriched in a given condition if they differed statistically significantly from the appropriate BioID2 only control (Fisher Exact, $p < 0.05$, Benjamini–Hochberg corrected). Individual protein levels in different samples were expressed relative to total BirA (biotin [acetyl-CoA-carboxylase] ligase) in the respective conditions, prior to further 2D vs. 3D fold-change enrichment analyses.

Proteins assigned to unreviewed UniProt entries within the enriched protein list were manually curated to identify if an appropriate reviewed entry exists. Proteins were reassigned to a reviewed entry if the sequence of an unreviewed entry was contained wholly within that of a reviewed entry or if the identified peptides were all contained within a reviewed entry. Entries which were contained in more than 33% of CRAPome controls were also excluded from the enriched list (Mellacheruvu et al., 2013) in addition endogenously biotinylated enzymes involved in metabolic carboxylation and decarboxylation reactions were removed from protein lists (Cronan, 1990). Enriched protein lists were manually curated on the basis of their UniProt annotation for subcellular localisation to remove extracellular matrix/region proteins. Enriched protein lists were also manually curated to ensure that duplicate entries were not present, for display purposes the total spectral counts were combined for the entries P14923 and B4DE59 (junction plakoglobin, JUP), and the entry for E9PCX8 (tensin-3 fragment) was excluded as 1030 of the 1041 spectra identified across all experiments were shared with Q68CZ2 (tensin-3, TNS3 (1717 total spectra)).

Visualisation of data and protein interaction networks was conducted using Cytoscape (version 3.7.1). Interaction networks were obtained from the STRING 10.5 database, interactions with a confidence score >0.4 on the basis of experimental and database evidence were included in the interaction network.

Paxillin/Git1/ β Pix/Myosin18A intensity

To determine intensity of paxillin, Git1, β Pix and Myosin18A in MDA-MB-231 and U2OS cells (treated as indicated) analysis of immunofluorescence images was conducted using the FIJI image analysis software. The image channel containing paxillin was processed to generate adhesion ROIs. The image was subtracted for background using the rolling ball method with a radius of 50. A Difference of Gaussians filter (GDSC ImageJ Toolsets) was then applied. The processed image was then used to generate an intensity threshold binary image, which was then used to define ROIs in the Git1/ β Pix channels. For object identification, a minimum size threshold of $0.5\mu\text{m}^2$ was used. These ROIs were then confirmed by visual observation and used to quantify fluorescence intensity.

Membrane proximal β Pix staining

To determine the proximity of β Pix in adhesions to cell edge/membrane versus whole adhesion, adhesions at cell periphery were examined for β Pix staining. Using Paxillin as a mask outline for the adhesion, a line scan across the whole adhesion was created. If there was signal above background levels for β Pix across whole paxillin signal this was classed as “whole adhesion” shown in black in bar graph; if there was signal only in membrane proximal region this was classed as “membrane-proximal” as shown in gray in bar graph.

Invasion assay (Cell Invasion Index)

To determine invasiveness of MDA-MB-231 cells (treated as indicated), first the integrated density of each optical section (Hoechst stain taken every $10\mu\text{m}$) was calculated using ImageJ. To calculate an invasion index score the sum of the integrated density of $40\mu\text{m}$ into the gel was divided by the negative sum of all invasive optical slices which was then normalised against the siNT control. $N = \geq 4$ independent experiments.

Circular invasion assay

MDA-MB-231 cells were imaged every 45 min for a 24–72h period. Three parameters were examined post image acquisition using ImageJ software, manually selected and using the “measure” tool. These parameters were: 1. Randomly selected single cell migration distance, tracking cells each time-point to the final time-point in focus. Distance traveled was measured using the measure tool. The total distance traveled was calculated over total time the cell was tracked for. 2. Randomly selected single cell migration speed, the same cells measured in 1 were used to calculate the speed. The speed was calculated from the distance traveled over the time measured, and 3. Randomly selected single cell protrusion lifetimes, the same cells were analyzed as in 1 and 2. The protrusion lifetime was the measurement of the total time that a protrusion (extension from cell body in the direction of travel) was present. Each data point shown are the protrusion lifetimes from individual cells over the time-course measured. $N = 33\text{--}35$ cells per condition, $N = 3$ independent experiments.

Wound healing analysis

Wound closure of U2OS cells (treated as indicated) was examined every 30min for a 40h period. Area of wound closure in every image acquired over 40h period, using ImageJ software. Data shown represents percentage of wound closure compared to time-point zero. Data represents N = 8–10 wound area per condition, N = 2 independent experiments.

Gelatin degradation

MDA-MB-231 cells (treated as indicated) were incubated for 24 h before fixing and staining with phalloidin and DAPI. Cells were imaged using spinning disk confocal microscopy. Following image acquisition cells were analyzed using ImageJ software. Two parameters were examined: 1. Percentage of cells in randomly (Roulette) selected ROI associated with one or more gelatin degradation spots, and 2. Number of degradation spots per cell. Data represents n = 157–217 cells per condition, N = 2 independent experiments.

Collagenase activity

MDA-MB-231 cells were incubated for 24h in DQ collagen/fibronectin gel before fixing and staining with phalloidin and DAPI. Cells were imaged using spinning disk confocal microscopy. Following image acquisition cells were analyzed using ImageJ software. Two parameters were examined: 1. Collagen/FITC intensity in whole ROI, and 2. Cell number through DAPI staining to ensure similar number of cells in each condition. Data represents n = 7–15 ROI per condition, N = 3 independent experiments.

Centrosome polarisation assay

MDA-MB-231 cells (treated as indicated) stained with SiR-tubulin were imaged overnight in collagen/fibronectin gels using spinning disk confocal microscopy. Following image acquisition cells were analyzed using ImageJ software. Cells were analyzed for migration, as described previously (Infante et al., 2018). Cells that showed migration were examined for centrosome location relative to nucleus, as shown in Figure 5C. Centrosomes at front quarter of nucleus were classed as polarised. Centrosomes in back three-quarters were classed as unpolarised. Data shown represents percentage of time centrosome was polarised during total length of migration in movie. N = 3 independent experiments; n = 27–39 cells.

Actin protrusion length

MDA-MB-231 cells (treated as indicated) were embedded in 3D matrices before staining with 200nM SiR-Actin (Cytoskeleton, Inc, cat#: SC001) for 2 h prior to imaging. Cells were imaged using spinning disk confocal microscopy. Following acquisition, length of actin protrusions were examined using ImageJ software, measuring the full length of actin protrusions from tip to cell body. n = 35–40 cells per condition, N = 3 independent experiments.

Nuclear circularity

Nuclear circularity of MDA-MB-231 cells (treated as indicated) was calculated using ImageJ software measuring the longest versus shortest axis of the nucleus in the direction of protrusion formation. Data represents n = 33–35 cells per condition, N = 3 independent experiments.

FRET data analysis

Analysis of raw images was conducted using the SlideBook 6 software (Intelligent Imaging Innovations, Inc) including the FRET module. Bleedthrough values for mTFP1 were determined using the 'Compute FRET Bleedthrough' functionality of the FRET module, imputing images of the mN2-TFP control construct taken under the same conditions as the mN2-tension sensor images. To analyze FRET readings at the nuclear envelope, and exclude non-specific readings, a mask was manually drawn over the NE signal (as visualised by the Acceptor channel). All measurements and bleedthrough calculations were then conducted using pixels within the mask, subtracting for background intensity that was calculated from a region outside of the cell that showed no specific fluorescent signal.

Presence of NM2A in protrusions

231-mNeonNM2A cells (treated as indicated) were embedded in 3D matrices before staining with 200 nm SiR-Actin (Cytoskeleton, Inc) for 2 h prior to imaging. Cells were imaged using spinning disk confocal microscopy. Following acquisition, NM2A and actin intensity was examined using ImageJ software following protocol outlined (www.unige.ch/medecine/bioimaging/files/1914/1208/6000/Quantification.pdf). NM2A in whole actin protrusion intensity was measured for "whole protrusion" quantification. Data shown represents actin intensity alone, NM2A intensity alone, and NM2A/actin ratio. Data represents N = 23–30 cells, N = 3 independent experiments. NM2A within 2 μ m of most distal region of protrusion tip.

Cytoplasmic/Perinuclear NM2A and NM2BMDA-MB-231 cells were embedded within 1.7 mg/mL collagen hydrogels supplemented with 50 μ g/mL fibronectin and cultured for 16 h prior to fixation and staining. Stained collagen gels were imaged on a 3i spinning disk confocal microscope, acquiring 40 slices 0.5 μ m apart. Slices were background subtracted before collapsing as a SUM intensity profile. A nuclear mask was generated from the DAPI stain, while a whole cell mask was generated from the phalloidin stain or NM2A stain. The perinuclear region was defined as a 5 μ m band around the nucleus. Rest of the cell was identified with phalloidin (for NM2B intensity) or NM2A (for NM2A intensity). Data represents n = 23–34 cells per condition, N = 3 independent experiments (NM2B experiments), n = 38–40 cells per condition, N = 4 independent experiments (NM2A experiments).

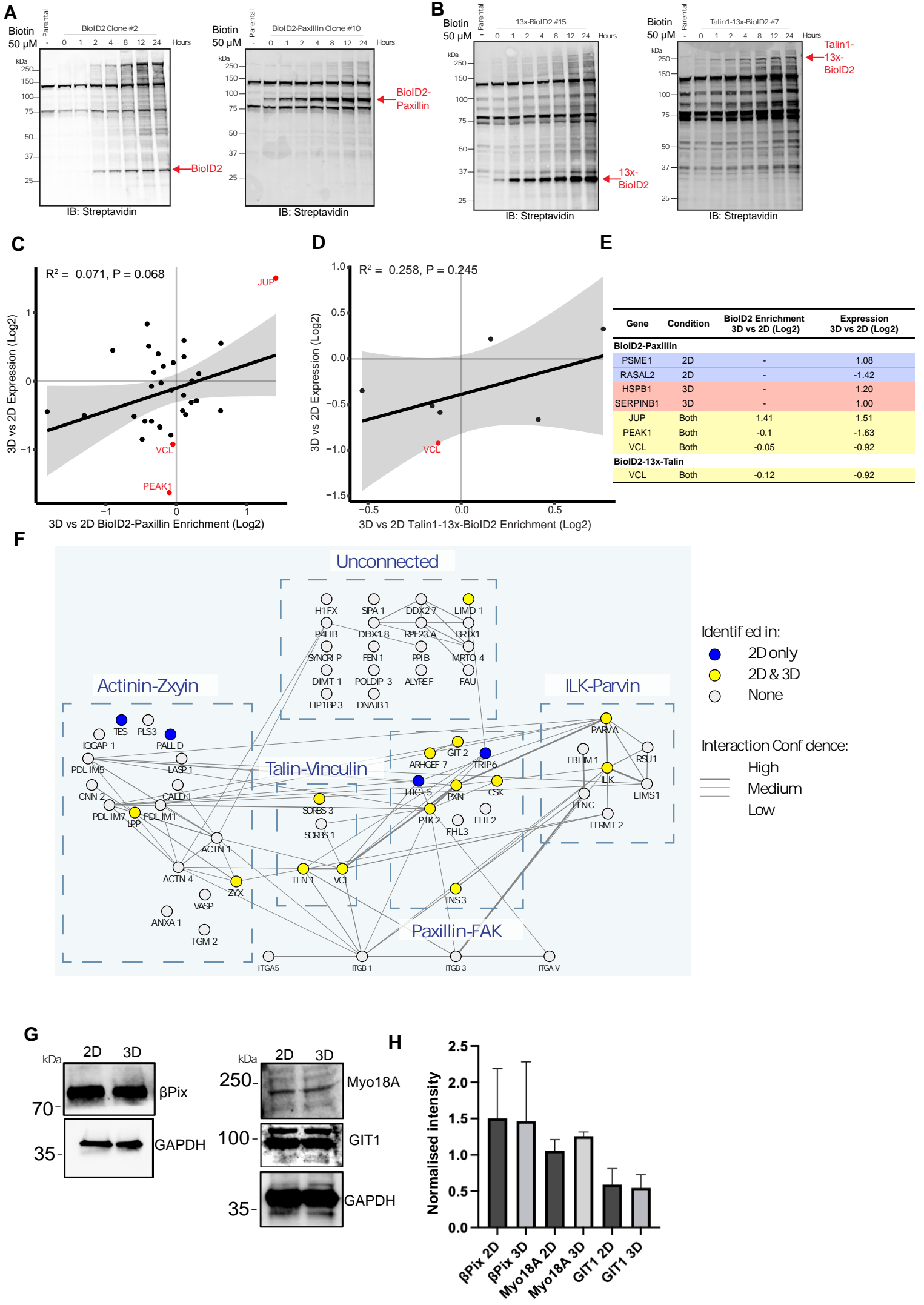
Cell Reports, Volume 42

Supplemental information

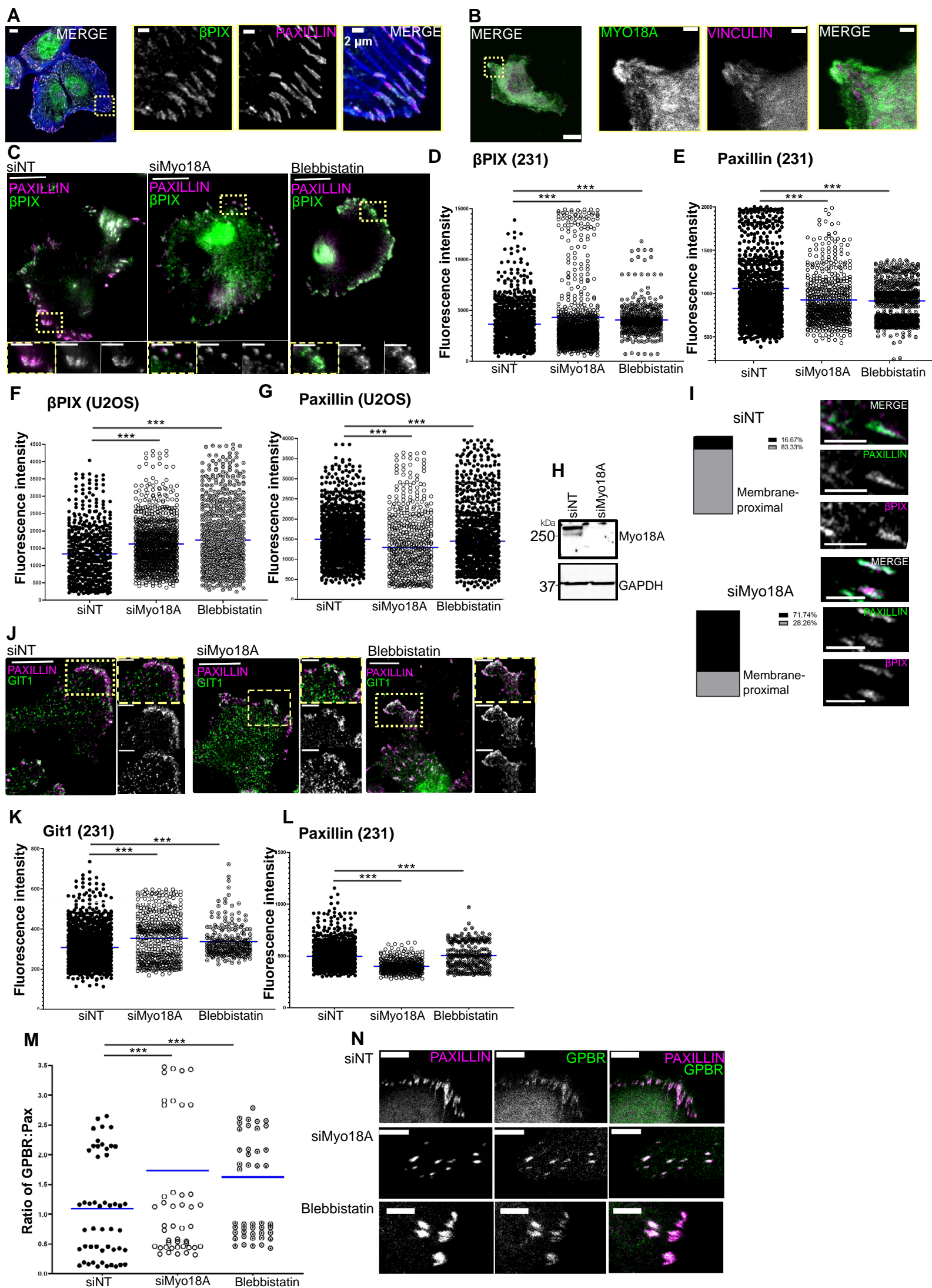
**3D matrix adhesion feedback
controls nuclear force coupling
to drive invasive cell migration**

Daniel Newman, Lorna E. Young, Thomas Waring, Louise Brown, Katarzyna I. Wolanska, Ewan MacDonald, Arthur Charles-Orszag, Benjamin T. Gault, Patrick T. Caswell, Tetsushi Sakuma, Takashi Yamamoto, Laura M. Machesky, Mark R. Morgan, and Tobias Zech

Supplementary Figure 1

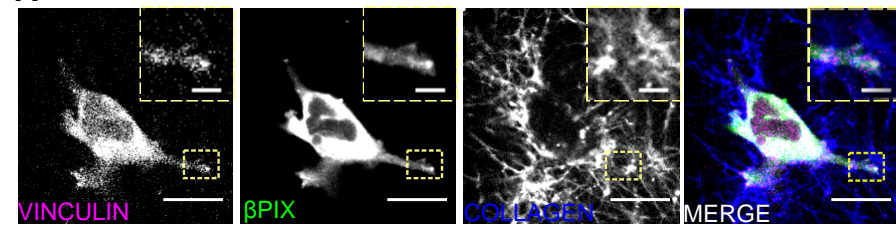


Supplementary Figure 2

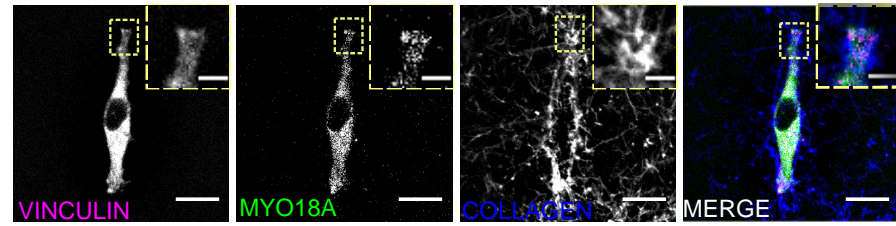


Supplementary Figure 3

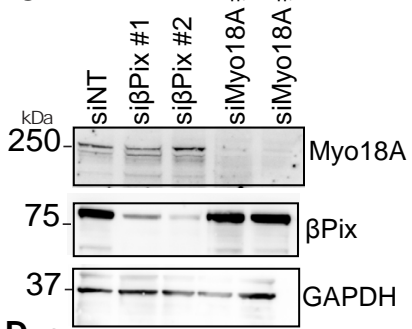
A



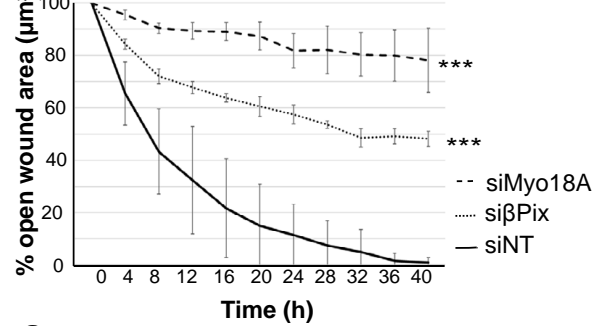
B



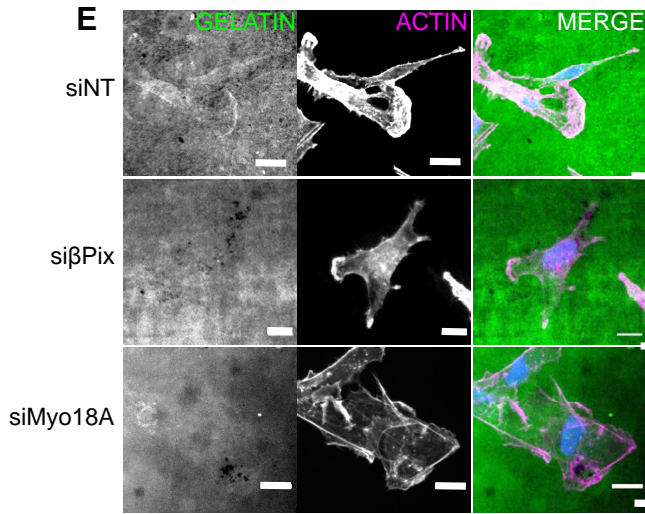
C



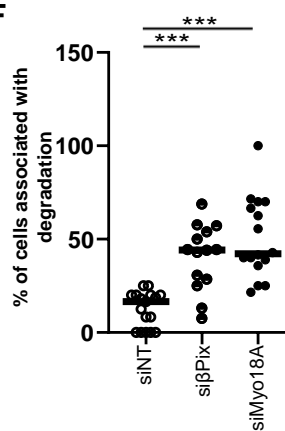
D



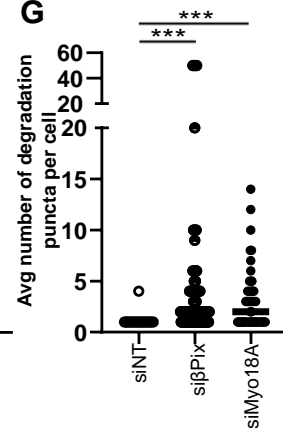
E



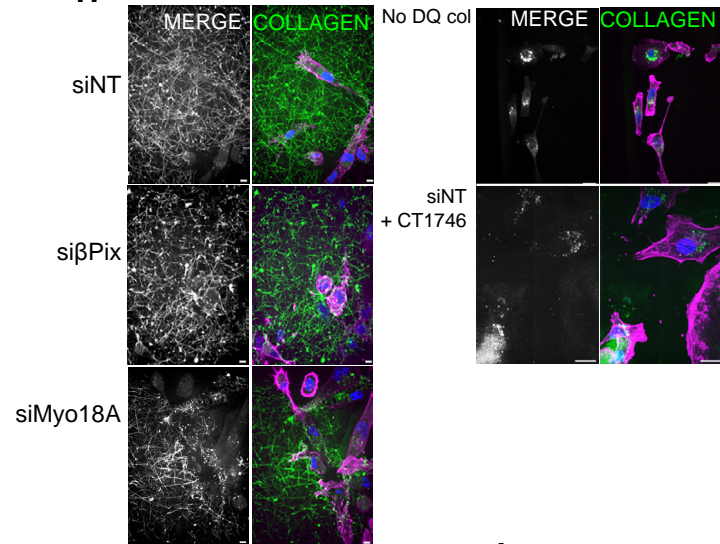
F



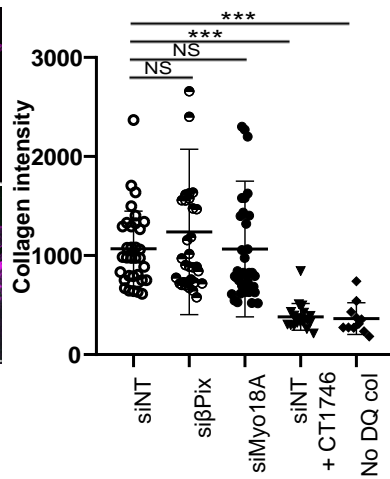
G



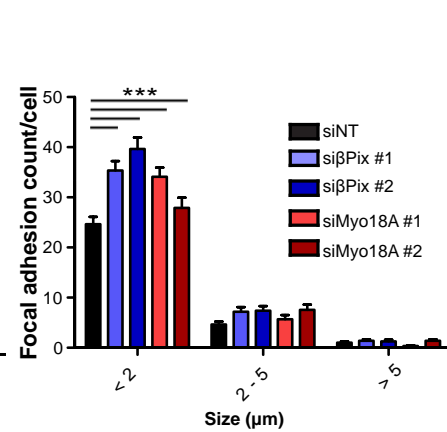
H



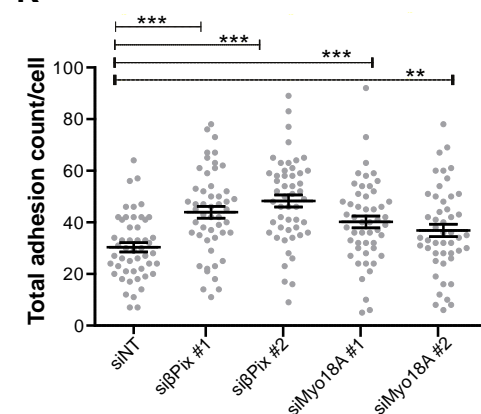
I



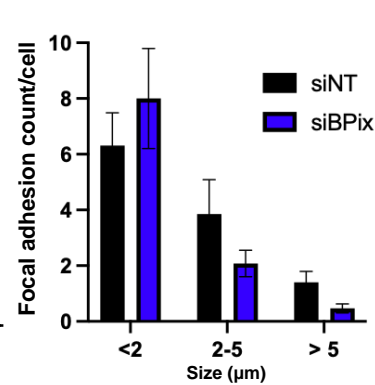
J



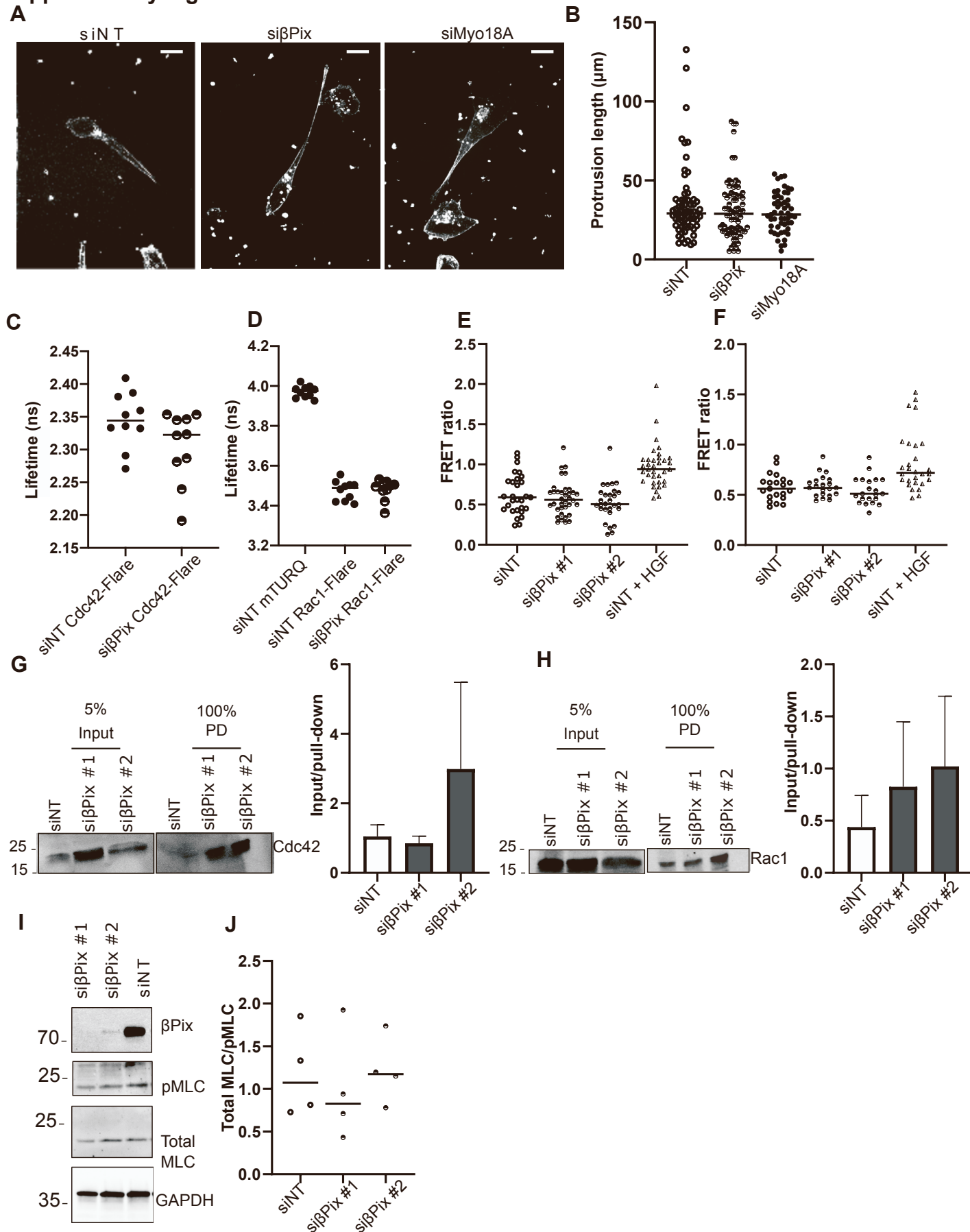
K



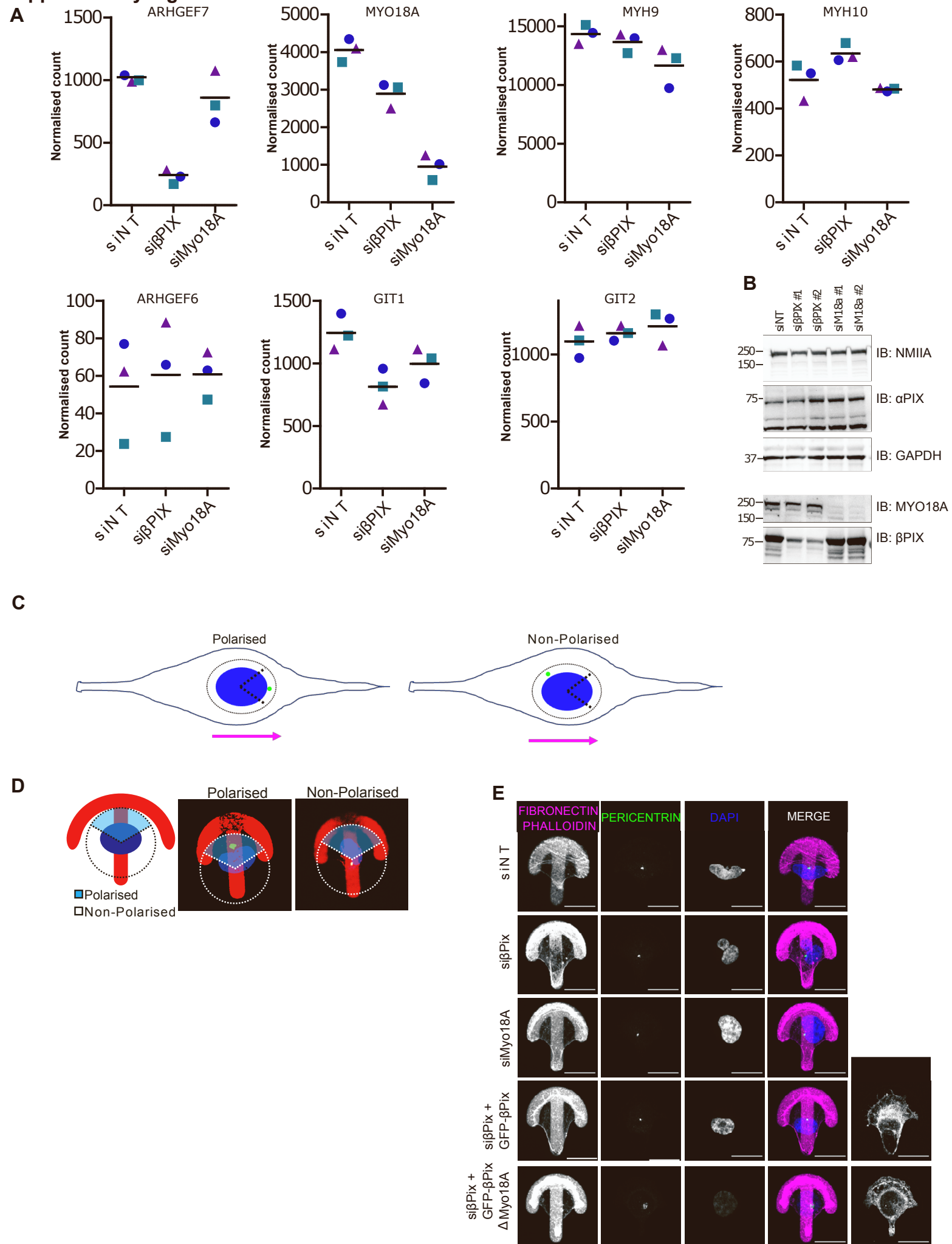
L



Supplementary Figure 4

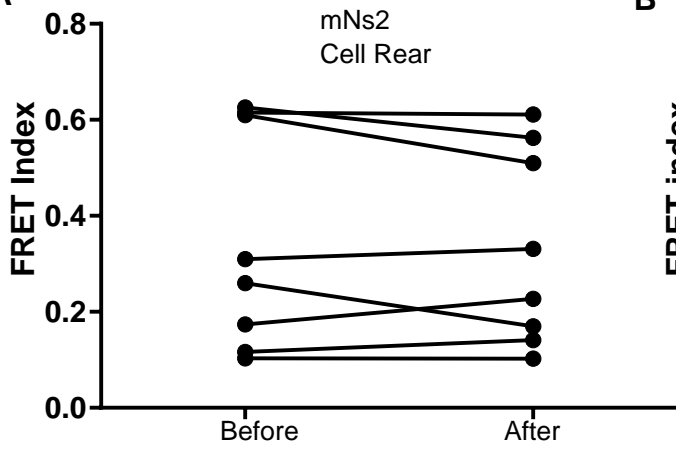


Supplementary Figure 5

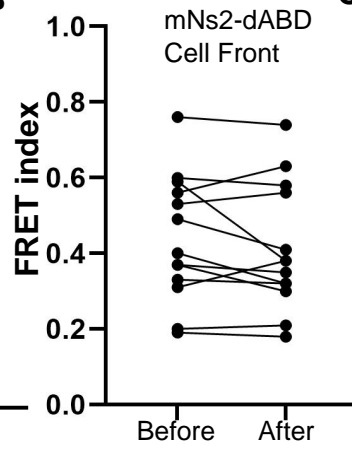


Supplementary Figure 6

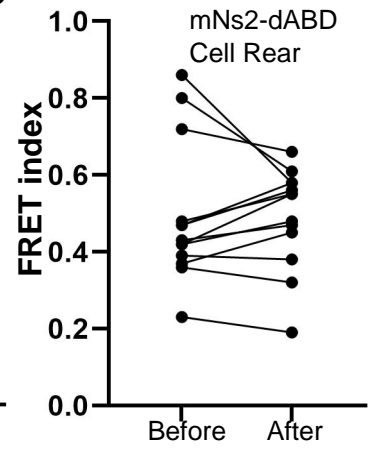
A



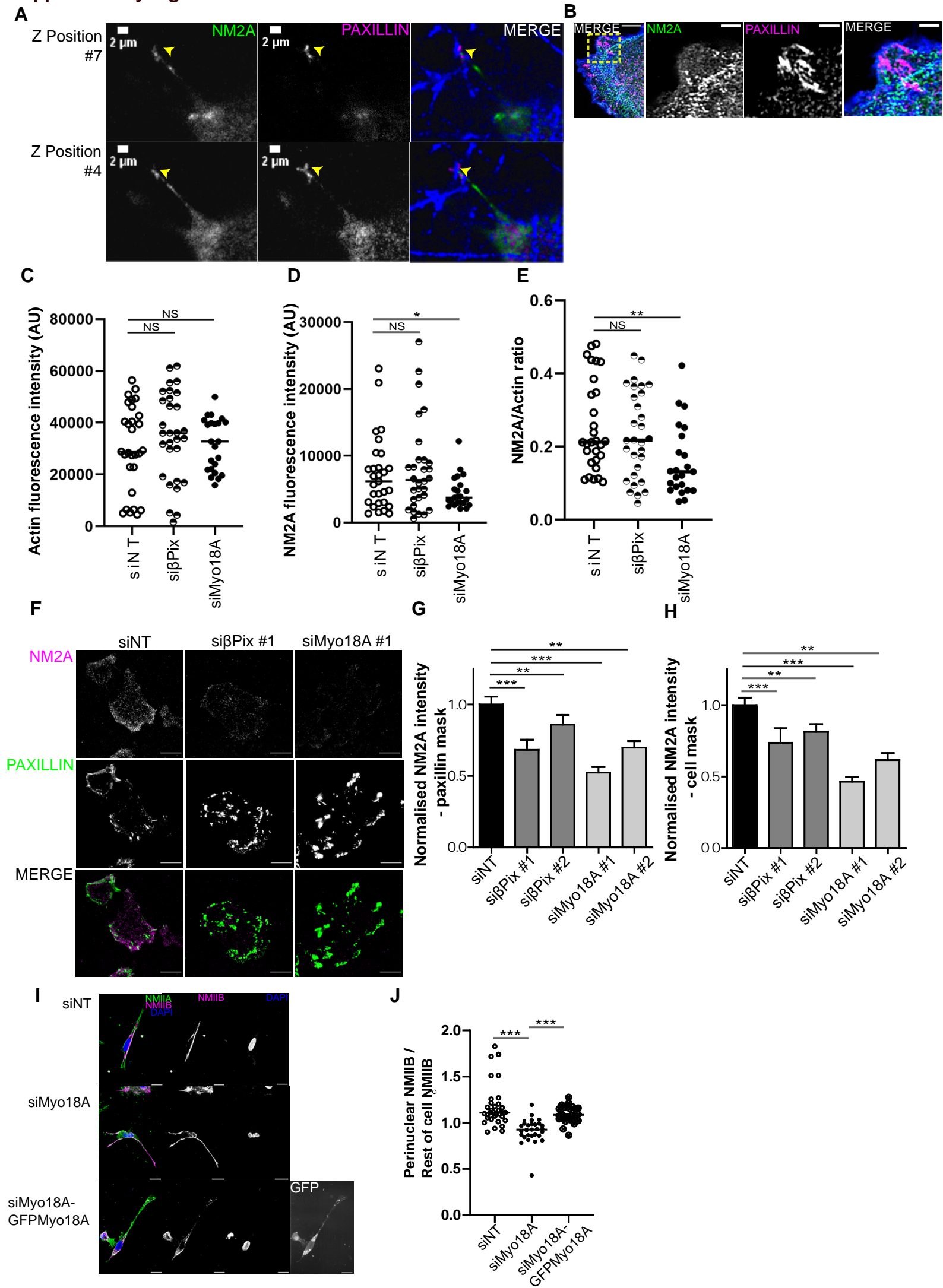
B



C



Supplementary Figure 7



Supplementary Figure 1. Comparison of IAC-associated proteins in MDA-MB-231 cells cultured in a 2D vs 3D microenvironment.

(A, B) Biotinylation time-course with indicated BioID2-expression constructs. Biotin incubation 50 μ M. (C, D) Expression changes identified in MDA-MB-231 cells cultured in 2D vs 3D by RNA-Seq. Scatterplots showing 3D vs 2D gene expression as assessed by RNA-Seq vs. 3D vs 2D protein enrichment in (C) BioID2-paxillin (D) talin1-13x-BioID2 datasets. Red points represent genes with expression changes that are statistically significant ($P < 0.05$, Benjamini-Hochberg corrected). (E) Table showing genes with statistically significant expression changes 3D vs 2D that were identified in either the BioID2-paxillin or talin1-13x-BioID2 datasets. (F) Diagram showing coverage of the 'consensus' adhesome (Horton et al., 2015) by the BioID2-paxillin & talin1-13x-BioID2 datasets. Blue dashed boxes enclose the 4 signalling axes described by Horton et al. Left to right: actinin-zyxin, talin-vinculin, paxillin-FAK, ILK-parvin; top: unconnected 'consensus' adhesome proteins. Interaction network obtained from STRING 10.5 (Experimental and Database interactions only, confidence > 0.4). Figure corresponds to Figure 1. (G) Western blot analysis of cell lysates generated from 2D vs 3D microenvironments. Western blot probed for β Pix, Git1, Myo18A and GAPDH (loading control). (H) Quantification of β Pix, Git1, Myo18A levels in 2D versus 3D microenvironments, compared with GAPDH loading control.

Supplementary Figure 2. Myo18A and actomyosin contractility are required for β Pix and Git1 localisation

(A) β Pix enriches in IACs in U2OS cells. Representative image of U2OS cells on fibronectin/collagen-coated coverslips, fixed and stained with phalloidin (blue), paxillin (magenta), and β Pix (green). Boxed region in expanded view indicates region of magnified view. Images are single Z slice projections. Scale bar in expanded view = 10 μ m, in magnified view = 2 μ m. (B) Representative image of MDA-MB-231 cells transfected with mCherry-Vinculin (magenta) and GFP-Myo18A (green) plated on fibronectin/collagen-coated coverslips. Boxed region in expanded view indicates region of magnified view. Images are single Z slice projections. Scale bar in expanded view = 10 μ m, in magnified view = 2 μ m. (C) Representative images of MDA-MB-231 cells on fibronectin/collagen-coated

coverslips treated with NT-siRNA, Myo18A-siRNA or treated with 20 μ M blebbistatin fixed and stained for paxillin (magenta), and β Pix (green). Scale bar in expanded view = 10 μ m, in magnified view = 5 μ m. (D) Quantification of fluorescence intensity of β Pix in paxillin staining mask in MDA-MB-231 cells treated with NT-siRNA, or Myo18A-siRNA or treated with 20 μ M blebbistatin. N = 3 independent experiments; n = 1088 - 1216 adhesions. Blue line indicates median value. One-way ANOVA; Dunnett's multiple comparison post-test versus NT-siRNA. p values: *** p < 0.001. (E) Quantification of fluorescence intensity of paxillin in MDA-MB-231 cells treated with NT-siRNA or Myo18A-siRNA or treated with 20 μ M blebbistatin. N = 3 independent experiments; n = 230-1241 adhesions. Blue line indicates median value. One-way ANOVA; Dunnett's multiple comparison post-test versus NT-siRNA. p values: *** p < 0.001. (F) Quantification of fluorescence intensity of β Pix in paxillin staining mask in U2OS cells treated with NT-siRNA or Myo18A-siRNA or treated with 20 μ M blebbistatin. N = 3 independent experiments; n = 602 - 1032 adhesions. Blue line indicates median value. One-way ANOVA; Dunnett's multiple comparison post-test versus NT-siRNA. p values: *** p < 0.001. (G) Fluorescence intensity of Paxillin in U2OS cells treated with NT-siRNA or Myo18A-siRNA or treated with 20 μ M blebbistatin. N = 3 independent experiments; n = 602 - 1032 adhesions. Blue line indicates median value. One-way ANOVA; Dunnett's multiple comparison post-test versus NT-siRNA. p values: *** p < 0.001. (H) Representative Western blot of MDA-MB-231 cells treated with NT-siRNA or Myo18A-siRNA. Western blot probed for Myo18A and GAPDH (loading control). (I) Bar chart showing β Pix staining in adhesions – membrane proximal (grey) or across whole adhesion (black) in cells treated with NT-siRNA or Myo18A-siRNA. Representative images of U2OS cells fixed and stained with Paxillin (magenta), and β Pix (green). (J) Representative images of MDA-MB-231 cells on fibronectin/collagen-coated coverslips treated with non-targeting- (NT) or Myo18A- siRNA or treated with 20 μ M blebbistatin fixed and stained with Paxillin (magenta), and Git1 (green). Scale bar in expanded view = 10 μ m, in magnified view = 5 μ m. (K) Fluorescence intensity of Git1 in paxillin staining mask in MDA-MB-231 cells treated with NT-siRNA, or Myo18A-siRNA or treated with 20 μ M blebbistatin. N = 3 independent experiments; n = 230-1241 adhesions. Blue line indicates median value. One-way ANOVA; Dunnett's multiple comparison post-test versus NT-siRNA. p values: *** p < 0.001. (L) Fluorescence intensity of paxillin in MDA-MB-231 cells treated with NT-siRNA or Myo18A-siRNA or treated with 20 μ M

blebbistatin. N = 3 independent experiments; n = 1088 - 1216 adhesions. Blue line indicates median value. One-way ANOVA; Dunnett's multiple comparison post-test versus NT-siRNA. p values: *** p < 0.001. (M) Fluorescence intensity ratio of Git1 paxillin binding region (GPBR) to Paxillin, in U2OS cells treated with NT-siRNA, or Myo18A-siRNA or treated with 20 μ M blebbistatin. n = 15 cells. N = 3 independent experiments. One-way ANOVA; Dunnett's multiple comparison post-test versus NT-siRNA. p values: *** p < 0.001. (N) Representative images of U2OS cells on fibronectin/collagen-coated coverslips treated with NT-siRNA, or Myo18A-siRNA or treated with 20 μ M blebbistatin fixed and stained with mApple-paxillin (magenta) and GPBR (green). Scale bar = 5 μ m. Corresponds to Figure 2.

Supplementary Figure 3. Loss of β Pix and Myo18A leads to an increase in nascent adhesions

(A) Representative image of MDA-MB-231 cells transfected with mCherry-vinculin (magenta) and GFP- β Pix (green) embedded in collagen (supplemented with ~1-2% fluorescent collagen (blue)) and fibronectin gel. Boxed region in expanded view indicates region of magnified view, circles in magnified view indicate paxillin/ β Pix enrichment. Scale bar in expanded view = 10 μ m, in magnified view = 2 μ m. (B) Representative image of MDA-MB-231 cells transfected with mCherry-vinculin (magenta) and GFP-Myo18A (green) embedded in collagen (supplemented with ~1-2% fluorescent collagen (blue)) and fibronectin gel. Boxed region in expanded view indicates region of magnified view. Scale bar in expanded view = 10 μ m, in magnified view = 2 μ m. (C) Representative Western blot of MDA-MB-231 cells treated with NT-siRNA, β Pix-siRNA, or Myo18A-siRNA. Western blot probed for Myo18A, β Pix-, and GAPDH (loading control). (D) U2OS cells treated with NT-siRNA, β Pix-siRNA, or Myo18A-siRNA were plated on 2D surfaces and underwent wound healing. Graph shows wound area measured 0 h - 40 h post wound. Data represents n = 8-10 wound

area per condition, N = 2 independent experiments. One-way ANOVA; Dunnett's multiple comparison post-test versus NT-siRNA to estimate p values: *** p < 0.001. (E) MDA-MB-231 cells treated with NT-siRNA, β Pix-siRNA, or Myo18A-siRNA and plated on FITC-labelled gelatin (green). Cells were fixed and stained for actin (magenta) and DAPI (blue) 24 h after seeding. Scale bar = 10 μ m. (F) Quantification of percentage of cells associated with one or more degradation spots under a cell. One-way ANOVA; Dunnett's multiple comparison post-test versus NT-siRNA to estimate p values: *** p < 0.001. (G) Quantification of average number of degradation areas formed per cell. Data represents n = 30-72 cells per condition, N = 2 independent experiments. One-way ANOVA; Dunnett's multiple comparison post-test versus NT-siRNA to estimate p values: *** p < 0.001. (H) Representative images of MDA-MB-231 cells treated with NT-siRNA, β Pix-siRNA, or Myo18A-siRNA or treated with 20 μ M CT1746 (MMP inhibitor) and embedded in DQTM collagen/fibronectin gels or gels containing no DQTM collagen. Scale bar = 20 μ m. (I) Dot plot to show collagen intensity of DQTM collagen from NT-siRNA, β Pix-siRNA, or Myo18A-siRNA, or 20 μ M CT1746, or no DQTM collagen treated cells. Data represents n = 7-15 ROI per condition, N = 3 independent experiments. One-way ANOVA; Dunnett's multiple comparison post-test versus NT-siRNA to estimate p values: *** p < 0.001. NS – Non-significant. (J) Histogram showing distribution of adhesion size based on adhesion number. Bonferroni corrected t-tests conducted within each bin comparing each NT-siRNA compared to β Pix-, or Myo18A- siRNA treated plated on 2D. (K) Total adhesion count per cell. One-way ANOVA; Dunnett's multiple comparison post-test versus NT-siRNA to estimate p values: *** p < 0.001. N = 5 independent experiments, n = 48-50 cells. (L) Distribution of adhesion size based on adhesion number in cells embedded in 3D, collagen/fibronectin gel mix. NT-siRNA compared to β Pix-siRNA, N = 3 independent experiments, n = 64-88 adhesions n = 18 cells.

Supplementary Figure 4. β Pix or Myo18A depletion does not affect protrusion assembly, Rho GTPase signalling or MLC phosphorylation

(A) Representative images of MDA-MB-231 cells treated with NT-siRNA, β Pix-siRNA, or Myo18A-siRNA embedded in collagen/fibronectin gels and stained with SiR-Actin. (B) Dot plot shows protrusion length of NT-, β Pix-, or Myo18A siRNA-treated cells. Data represents N = 35-40 cells per condition, N = 3 independent experiments. (C, D)

MDA-MB-231 cells treated with NT-siRNA or β Pix-siRNA and transfected with Rac (C) or CDC42 FLARE (D) constructs were imaged using FLIM, $n = 10$ cells in $N = 3$. (E, F) MDA-MB-231 cells treated with NT-siRNA, β Pix-siRNA #1 or β Pix-siRNA #2, and transfected with Rac (E) or CDC42 (F) FRET constructs and imaged using FRET setup, $n = 28-35$, cells in $N = 3$. (G) Rac1 and (H) Cdc42 levels in MDA-MB-231 cells treated with NT-siRNA, β Pix-siRNA. Cells were lysed 96 h after first siRNA treatment, and Rac1 or Cdc42 were pulled down with GST-PBD-Sepharose beads. Equal amounts of protein were subjected to western blot analysis, which were probed for anti-Rac1 and anti-Cdc42.

(I) Western blot analysis of whole cell lysates from MDA-MB-231 cells treated with NT-siRNA, β Pix-siRNA #1 or β Pix-siRNA #2, probed for β Pix, pMLC, total MLC, or GAPDH. (J) Quantification of pMLC/MLC levels from cell lysates as in (I).

Supplementary Figure 5. RNA-Seq analysis and Western blot analysis following β Pix- or Myo18A- depletion

(A) Normalised counts of selected genes from RNA-Sequencing analysis of MDA-MB-231 cells embedded in 3D Collagen treated with pooled siRNA oligos. $N = 3$, Coloured shapes represent individual replicates. ARHGEF7 – β Pix protein, MYO18 – Myo18A protein, MYH9 – NM2A heavy chain protein, MYH10 – NM2B heavy chain protein, ARHGEF6 - α PIX protein, GIT1 – GIT1 protein, GIT2 – GIT2 protein.

(B) Western blot analysis of MDA-MB-231 cells embedded in 3D Collagen treated with indicated siRNA oligos. (C) Schematic of scoring system used for migrating polarisation assessment. Cells were considered to be polarised if the centrosome (green dot) was located in the front third of the cell, in front of the nucleus. Cells were considered to be unpolarised if the centrosome was in the back two thirds of the cell. Magenta arrow indicates direction of migration. (D) Schematic of scoring system used for polarisation assessment. Cells were considered to be polarised if the centrosome (green dot) was located in the front third of the cell, in front of the nucleus. Cells were considered to be unpolarised if the centrosome was in the back two thirds of the cell. (E) Representative maximum projections of cells on CYTOO crossbow chip stained with phalloidin (magenta), pericentrin (green), DAPI (blue), treated with NT-siRNA, β Pix-siRNA, or Myo18A-siRNA, untransfected or transfected with GFP- β Pix or GFP- β Pix/Myo18A binding

mutant. Scale bar = 20 μ m. Figure corresponds to Figure 3.

Supplementary Figure 6. Control measurements of mini-nesprin-2 tension sensor and nesprin-tension sensor lacking N-terminal actin binding domain during migration.

(A) Confocal imaging of MDA-MB-231 cells expressing mNs2 (mini-nesprin2 tension sensor) in 3D environments (2 mg/mL collagen). Average FRET index of the rear face of the nucleus before and after translocation for 7 cells. N = 4 experiments. $p= 0.741$, paired t-test. Figure corresponds to Figure 4. (B and C) Confocal imaging of MDA-MB-231 cells expressing Nesprin-tension sensor lacking N-terminal actin binding domain (mNs2-dABD) in 3D environments (2 mg/mL collagen). Average FRET index of the front (B) rear (C) face of the nucleus of cells expressing mNs2-dABD before and after translocation for 8 cells. Figure corresponds to Figure 4.

Supplementary Figure 7. NM2A accumulates at adhesive sites in 3D-embedded cells

(A) CRISPR-generated NM2A-mNeon (green) MDA-MB-231 knock-in cells embedded in collagen (supplemented with ~1-2% fluorescent collagen, (blue)) and fibronectin gels were fixed and stained for paxillin (magenta). Images represent single Z slice projections at two different positions. Adhesive sites are indicated with yellow arrowhead. Corresponds to Figure 5. (B) CRISPR-generated NM2A-mNeon (green) MDA-MB-231 knock-in cells plated on fibronectin/collagen-coated coverslips were fixed and stained for Paxillin (magenta) and phalloidin (blue). Image on left panel is expanded view, yellow boxed region indicates zoom region shown on right. Scale bar expanded = 5 μ m, zoom = 2 μ m. (C-E) NM2A-mNeon (green) MDA-MB-231 knock-in cells treated with NT-siRNA, β Pix-siRNA, or Myo18A-siRNA. embedded in collagen/fibronectin gels were stained with SiR-Actin and imaged by confocal microscopy. Dot-plots show fluorescence intensity of actin (C) and NM2A (D) along the length of the actin protrusion. (E) Ratio of actin:NM2A intensity calculated from data shown in B,C. n = 23-30 cells, N = 3 independent experiments. One-way ANOVA; Dunnett's multiple comparison post-test versus NT-siRNA to estimate p values: NS -

not significant, ** $p < 0.01$, * $p < 0.05$. Figure corresponds to Figure 5. (F) NM2A staining on 2D surfaces. Representative TIRF images of MDA-MD-231 cells treated with NT-siRNA or β Pix-siRNA plated on fibronectin/collagen-coated coverslips fixed and stained for NM2A (green) and paxillin (magenta). Scale bar = 10 μ m. (G) Average NM2A intensity within paxillin based adhesion mask. (H) Average NM2A intensity within cell based mask. One-way ANOVA; Dunnett's multiple comparison post-test versus NT-siRNA to estimate p values: NS - not significant, ** $p < 0.01$, *** $p < 0.001$. N = 5, cells n=48–50. (I) Representative images of MDA-MB-231 cells treated with NT-siRNA or Myo18A-siRNA +/- GFP-Myo18A embedded in collagen/fibronectin gels stained for DAPI (blue), NM2A (green), and NM2B (magenta). Scale Bar = 20 μ m. (J) Perinuclear NM2B intensity as a ratio of whole cell NM2B intensity. One-way ANOVA; Dunnett's multiple comparison post-test versus NT-siRNA to estimate p values: *** $p < 0.001$. Data represents n = 23-34 cells per condition, N = 3 independent experiments. Figure corresponds to Figure 5 and 6.

Supplementary Movie 1-3:

MDA-MB-231 cells treated with NT-siRNA (Movie 1), β Pix-siRNA (Movie 2), or Myo18A-siRNA (Movie 3) undergoing Circular Invasion Assays for 24-48h. Movies show examples of cells tracked over-time. Corresponds to Figure 3.

Supplementary Movie 4-6:

MDA-MB-231 cells stained with SiR-tubulin embedded in collagen/fibronectin gels, treated with NT-siRNA (Movie 4), β Pix-siRNA (Movie 5), or Myo18A-siRNA (Movie 6). Magenta arrow indicates cell migration direction. Scale bar 10 μ m. Corresponds to Figure 3.

Supplementary Movie 7: NM2A accumulates early in new protrusions MDA-231-2A cell expressing NM2A-mNeon (green) cells transfected with mApple-paxillin (magenta) embedded in collagen supplemented with 1-2% fluorescent collagen (blue) & fibronectin gels. Cells were imaged by live cell microscopy at 2 min intervals. Scale bar 2 μ m. Corresponds to Figure 5.